SPECTRAL RADIATIVE PROPERTIES OF THIN FILMS WITH ROUGH SURFACES USING FOURIER-TRANSFORM INFRARED SPECTROMETRY

A Thesis
Presented to
The Academic Faculty

by

Vinh P. Khuu

In Partial Fulfillment
of the Requirements for the Degree of
Master of Science in the
Woodruff School of Mechanical Engineering

Georgia Institute of Technology
May 2004

SPECTRAL RADIATIVE PROPERTIES OF THIN FILMS WITH ROUGH SURFACES USING FOURIER-TRANSFORM INFRARED SPECTROMETRY

A Thesis
Presented to
The Academic Faculty

by

Vinh P. Khuu

In Partial Fulfillment
of the Requirements for the Degree of
Master of Science in the
Woodruff School of Mechanical Engineering

Georgia Institute of Technology
May 2004

SPECTRAL RADIATIVE PROPERTIES OF THIN FILMS WITH ROUGH SURFACES USING FOURIER-TRANSFORM INFRARED SPECTROMETRY

Approved by:

Dr. Zhuomin Zhang, Advisor

Dr. Andrei G. Fedorov

Dr. J. Robert Mahan

April 12, 2004

ACKNOWLEDGMENTS

First, I would like to thank my advisor, Dr. Zhuomin Zhang, for taking me on as a graduate research assistant and for providing valuable support and help throughout the course of my research. I thank him for his commitment and for always expecting my best.

I gratefully acknowledge Dr. J.R. Mahan, who provided encouragement, advice, and support during my stay at Georgia Tech Lorraine. I also appreciate his willingness to serve on my thesis committee. I also thank Dr. Andrei Fedorov for serving on my thesis committee.

The support provided by the heat transfer research group was wonderful. All group members helped me with my research in some way. In particular I would like to thank Bong Jae Lee for a fruitful collaboration during the fall semester, which made possible much of the work presented in this thesis. Ceji Fu offered valuable discussion and suggestions for reviewing this manuscript. I acknowledge Yu-Bin Chen for his help in providing me with the profilometer and microscope data and for cutting the silicon wafers and Qunzhi Zhu for obtaining the AFM measurements. I also appreciate Dan McCormick's help in reviewing this thesis.

Finally, I would like to thank my family, especially my parents, who have encouraged and supported me throughout my undergraduate and graduate careers. I am grateful for the freedom to carry out my studies without hindrance, wherever that journey has brought me.

TABLE OF CONTENTS

LIST OF TABLES

LIST OF FIGURES

NOMENCLATURE

A	projected area of beam on detector
B	spectrum (in frequency domain)
d	thicknesse
E	electric field or throughput
h	surface height
I	incident radiation intensity or interferogram
i	$\sqrt{-1}$
j	medium index
j'	medium index
L	total sampling length
M	maximum number of data points
n	real part of complex refractive index
R	reflectance
r	reflection Fresnel coefficient
S	scattering factor
T	transmittance
$\overline{T}$	fringe-averaged transmittance
t	time or transmission Fresnel coefficient
u	velocity of moving mirror
x	horizontal position

Greek symbols

β	phase shift
δ	penetration depth or retardation
κ	imaginary part of complex refractive index
θ_2	angle of incidence
λ	wavelength
$\delta\overline{\nu}$	coherent spectral width
$\Delta\overline{\nu}$	free spectral range
$\overline{\nu}$	wavenumber
σ	surface roughness, or standard deviation
τ	internal transmittance, or autocorrelation length
Φ	fringe contrast
ϕ	coherence function
Ω	solid angle
ω	angular frequency

Subscripts

c	calculated
coh	coherent
f	film
hc	half cone
m	measured
max	maximum

min	minimum
p	*p*-polarized
rms	root-mean-square
s	*s*-polarized
1	air
2	film

SUMMARY

Thin films are used in many energy conversion applications, ranging from photodetectors to solar cells. Accurately predicting the radiative properties of thin films when they possess rough surfaces is critical in many instances, but can be challenging due to the complexity arising from light scattering and interferences at the microscale. This work describes measurements of the spectral transmittance and reflectance of several thin-film materials (including crystalline silicon wafers and a polycrystalline diamond film) in the mid-infrared spectral region (2 – 20 μm) using a Fourier-transform infrared (FT-IR) spectrometer. The transmittance and reflectance were calculated using thin-film optics for the double-side polished samples and scalar scattering theory for the single-side polished samples. The effects of partial coherence are considered using a fringe smoothing technique. The interval used for fringe smoothing was assumed to be linearly dependent on the wavenumber. Good agreement between the predicted and measured transmittance was achieved for the double-side polished silicon wafers and for the diamond film. The disagreement for some single-side polished silicon wafers may be inherently related to their surface microstructures, as suggested from surface topographic data and images obtained from surface profilometry and microscopy. By comparing the intervals used for fringe smoothing with the instrumental resolution, beam divergence in the spectrometer was found to be a major factor contributing to the partial coherence. Future research is proposed to investigate the correlation between the detailed surface characteristics and the conical-conical transmittance and reflectance.

CHAPTER 1

INTRODUCTION

Thin solid films are well-known for their applications in electronics and optics, particularly in integrated circuits and optical filters. Increasingly, they are attracting the attention of mechanical engineers because of their potential for energy conversion and energy transfer. One active area of research is thin film solar cells, which can have textured surfaces to enhance absorption (Poruba et al., 2000). Polycrystalline silicon solar cells are now being engineered to have varying levels of optical transparency, making them suitable for applications in architecture and the automobile industry (Boueke et al., 2001). Thermophotovoltaic devices, which convert thermal radiation into electrical energy, possess similarities with conventional photovoltaic devices and hold promise as a low-cost alternative to solar cells (Coutts, 1998). High-temperature superconducting (HTSC) thin films have unique radiative properties in the far-infrared spectral region, which can be useful in the design of infrared detectors, phase modulators, and radiation shields (Kumar et al., 1999).

The existence of rough surfaces can enhance the optical and radiative properties of thin films in energy conversion devices. A thorough understanding of the radiative properties of thin films is important for developing reliable models for their use in industrial applications. Accurately predicting the transmittance and reflectance can be challenging due to the complexity arising from light scattering and interference at the microscale. Currently, the effective medium approximations (EMA) and scalar scattering theory are the two most commonly-used approaches for treating the rough surface effects (Petrich and Stenzel, 1994; Fujiwara et al., 2000). Previous studies showed that scalar

scattering theory could yield reasonable agreement with certain experiments; however, the applicability to various surface conditions has not been established. For instance, using scalar scattering theory, Petrich and Stenzel (1994) only focused on CVD diamond layers on silicon substrates that had rms surface roughnesses below 100 nm in the 4000 – 8000 cm^{-1} wavenumber range. An approach based on perturbation theory used by Montecchi et al. (2001) proved to be effective in modeling the radiative properties of LiF thin films with rough surfaces in the 5000 – 31000 cm^{-1} wavenumber range. The applicability to other common semiconductor materials, such as silicon, has yet to be explored. Poruba et al. (2000) used scalar scattering theory to optically characterize silicon thin films to study the origins of enhanced light absorption in solar cells. These samples were hydrogenated microcrystalline silicon deposited by a very high frequency glow discharge technique, which may have different radiative properties than commercial silicon wafers.

Furthermore, neither scalar scattering theory nor the EMA models by themselves consider partial coherence, a thorough understanding of which is needed to accurately model the radiative properties of many thin films. Partial coherence theory, which describes the electromagnetic fields, has been successfully applied to smooth thin films in many studies (Chen and Tien, 1992; Zhang, 1994; Grossman and McDonald, 1995). Grossman and McDonald (1995) studied the wavenumber dependence of partial coherence in addition to instrumental effects on FT-IR data, but only for smooth dielectric lamellae. Spectral averaging, an alternative approach to addressing partial coherence, has been shown to produce equivalent results to partial coherence theory (Chen and Tien, 1992), but its value has yet to be discussed in-depth in the literature.

Scalar scattering theory combined with spectral averaging to address the partial coherence has yet to be applied to silicon wafers and diamond thin films, two common semiconductor materials. An attempt to model their transmittance and reflectance in the mid-infrared spectral range, a region of importance in many applications, is undertaken in this study. This thesis addresses many issues surrounding the problem of accurately modeling and measuring the radiative properties, specifically: (i) How does FT-IR spectrometry work, and what precautions can be taken to help ensure accurate measurements? (ii) What insights can be gained by addressing partial coherence using spectral averaging? and (iii) What are the effects of rough surfaces on the transmittance and reflectance, and how effective is scalar scattering theory at modeling these effects?

In order to investigate these issues, the following methodology is used. The spectral transmittance and reflectance of several thin-film materials (including crystalline silicon wafers and polycrystalline diamond thin film) are measured in the mid-infrared spectral region (500 – 5000 cm^{-1}) using Fourier-transform infrared (FT-IR) spectrometry. An atomic force microscope, a surface profilometer, and an optical microscope provide topographic data used to fully characterize the rough surfaces. The transmittance and reflectance are calculated using tabulated optical constant data along with either thin-film optics for the double-side polished samples or scalar scattering theory for the single-side polished samples. Scalar scattering theory is used in the present study because of its inherent advantages in addressing the effects of roughness on the transmittance (Carniglia and Jenson, 2002). Film thickness and surface roughness are taken as adjustable parameters to fit the calculated spectra to the measurements. Fringe smoothing, which addresses the partial coherence of the radiation, is employed to improve the agreement.

The predicted spectra obtained from the fitting process can then be compared to the measured spectra. The wavenumber dependence of the degree of coherence is also studied.

The work is organized as follows. Chapter 2, which focuses on theory, discusses scalar scattering theory and its advantage over other methods that treat roughness of surfaces. An analysis of spectral averaging serves as the foundation for a discussion of partial coherence. Chapter 3 describes the fundamentals of FT-IR spectrometry and discusses ways to ensure accurate measurements. Details about the spectrometer and measurement conditions are also provided. Chapter 4 presents the results of the measurements. The analysis addresses the different factors contributing to partial coherence of the radiation, such as sample characteristics and instrumental effects. Finally, Chapter 5 summarizes the important results and gives recommendations toward better understanding the surface characteristics and the conical-conical transmittance and reflectance for modeling the spectral radiative properties of thin solid films with rough surfaces.

CHAPTER 2

THEORY

2.1 Introduction

One of the important characteristics of thin films is that the thicknesses are sufficiently small that interference effects are apparent in the spectrum. The term "thin film" can often seem vague, however, and whether a given layer is thin enough to be considered "thin," depends on many factors. In a "thick film," the interference can be neglected, which is generally possible when the thickness is much greater than the wavelength of the incident radiation. It has been suggested that the coherent length, which depends on the spectral width of the source and the spectrometer's resolution, should be used rather than the wavelength, which could be much less than the coherent spectral width (Zhang et al., 2003). The penetration depth, $\delta = \lambda / 4\pi\kappa$, where κ is the imaginary part of the complex index of refraction and λ is the wavelength, is another indicator to help determine whether interference needs to be considered. This value can be compared with the thickness and if it is much smaller, the condition for a thin film is satisfied, and using the thin film equations is recommended.

For many reasons, it may happen that the surfaces of a thin film are rough. Commercial thin silicon wafers, for instance, are usually available in a variety of surface finishes: as-cut, etched, lapped, or polished and as such can have rough surfaces. Understanding the effects of surface roughness can be critical toward predicting their radiative behavior. Several approaches have been developed over the years to predict the effects on the transmittance and the reflectance. These approaches can be classified into four main groups: (i) diffraction theories, (ii) classical scattering and perturbation

theories, (iii) first principle theories based on the electromagnetic response of systems having spatial fluctuations, and (iv) effective medium theories with surface layer optical models (Fujiwara et al., 2000). Of these, scalar scattering theory and the effective medium approximations appear to be the most commonly used and have yielded good agreement with measurements in some cases (Poruba et al., 2000; Fujiwara et al., 2000).

Scalar scattering theory, which accounts for the losses of the energy in the specularly reflected or transmitted beams using modified Fresnel coefficients, has been applied in numerous studies since the 1960s (Beckman and Spizzichino, 1987). Filinski (1972), for instance, modeled roughness as a plane of surface irregularities that give rise to phase disturbances, which were used to explain the reduction in the transmitted and reflected radiant power. Mitsas and Siapkas (1995) developed a general matrix method to treat coherent, partially coherent, and incoherent multiple reflections in a multilayer structure on a thick substrate. Montecchi et al. (2001) incorporated the effects of inhomogeneity, surface roughness, and non-parallelism of the surfaces to model the radiative properties of a LiF film on a glass substrate and obtained excellent agreement with the measurements. The importance of optically characterizing efficient thin-film solar cells led to a study of bulk and surface scattering by Poruba et al. (2000), who showed that the enhanced light absorption used in microcrystalline silicon thin films is primarily due to scattering at the textured, rough surfaces.

The effective-medium approximation (EMA), also known as the effective-medium theory (EMT), is the other commonly used method for treating rough thin films. It assumes a thin homogenous layer with intermediate values for the refractive index in place of a rough surface in order to account for the reduction in the reflectance. The

effective medium class of theories can be further divided into formulations based on the dielectric function model used to determine the refractive index of the intermediate layer. Because most effective medium approximations are based on models of light reflection and often assume a nonabsorbing transition layer, they are ideally suited toward reflectometry and ellipsometry (Fujiwara et al., 2000). Indeed, a major drawback to using EMT model is the limited accuracy of modeling the transmittance. Recently, Carniglia and Jensen (2002) showed that an EMA model with an absorbing transition layer, which accounts for the decrease in the transmittance, is equivalent to scalar scattering theory in predicting the decrease in the spectral reflectance and transmittance due to rough surfaces. The inherent advantages with regard to transmittance, a major component of this work, led to the decision to use scalar scattering theory.

2.2 Scalar Scattering Theory

Scalar scattering theory is a powerful tool for modeling the transmittance and reflectance of thin films with rough surfaces and can also be used to extract optical constants and geometrical parameters, such as film thickness and root-mean-square (rms) surface roughness. The coherent formulation combined with modified Fresnel coefficients form the basis of scalar scattering theory. Figure 2.1 shows the beam geometry and sample structure. A dielectric layer of average thickness d with internal absorption but no internal scattering is immersed in ambient air. Because the extinction coefficient κ_2 of the dielectric material is usually much smaller than the refractive index n_2, the slightly absorbing model proposed by Zhang (1999) can be applied. Consequently, Airy's formulas for thin films can be used to approximate the reflection and transmission coefficients as follows (Modest, 2003):

$$r = r_{12} + \frac{t_{12}t_{21}r_{23}\tau e^{i2\beta}}{1 - r_{21}r_{23}\tau e^{i2\beta}} \tag{2.1}$$

$$t = \frac{t_{12}t_{23}\sqrt{\tau}e^{i\beta}}{1 - r_{21}r_{23}\tau e^{i2\beta}} \tag{2.2}$$

where the phase shift $\beta = \frac{2\pi n_2}{\lambda} d\cos\theta_2$ and the internal transmissivity $\tau = \exp\left(-\frac{4\pi\kappa_2}{\lambda}\cdot\frac{d}{\cos\theta_2}\right)$. Here, n_2, κ_2, and d are the refractive index, extinction coefficient, and thickness of the sample, respectively, and $\theta_2 = \sin^{-1}(n_1 \sin\theta_1 / n_2)$, given by Snell's law.

In order to model the loss in the reflected or transmitted energy in the specular direction due to scattering, the Fresnel coefficients are modified with scattering factors, which depend on the rms surface roughness. The exact form of these factors results from assuming that the rms roughness of the surfaces follows a Gaussian distribution. Under the slightly absorbing assumption, the modified Fresnel coefficients at the interface between medium j and j' ($j = 1, 2$ or 3; $j' = j \pm 1$) for *p*-polarization are

$$r_{p,jj'} = \frac{n_j \cos\theta_{j'} - n_{j'}\cos\theta_j}{n_j \cos\theta_{j'} + n_{j'}\cos\theta_j} S_{r,jj'} \tag{2.3}$$

$$t_{p,jj'} = \frac{2n_j \cos\theta_j}{n_j \cos\theta_{j'} + n_{j'}\cos\theta_j} S_{t,jj'} \tag{2.4}$$

Similarly, the modified Fresnel coefficients for *s*-polarization are

$$r_{s,jj'} = \frac{n_j \cos\theta_j - n_{j'}\cos\theta_{j'}}{n_j \cos\theta_j + n_{j'}\cos\theta_{j'}} S_{r,jj'} \tag{2.5}$$

$$t_{s,jj'} = \frac{2n_j \cos\theta_j}{n_j \cos\theta_j + n_{j'} \cos\theta_{j'}} S_{t,jj'} \tag{2.6}$$

In the above equations, the scattering factors are the same for both polarizations (Beckmann and Spizzichino, 1987):

$$S_{r,jj'} = \exp\left[-\frac{1}{2}\left(\frac{4\pi n_j \sigma_{jj'} \cos\theta_j}{\lambda} \right)^2 \right] \tag{2.7}$$

$$S_{t,jj'} = \exp\left[-\frac{1}{2}\left(\frac{2\pi (n_j - n_{j'}) \sigma_{jj'} \cos\theta_j}{\lambda} \right)^2 \right] \tag{2.8}$$

where $\sigma_{jj'}$ is the rms roughness of the interface between medium j and j'. The first and third media are identical (air), and the spectral reflectance and transmittance can be calculated for each polarization using the following equations:

$$R = r\, r^* \tag{2.9}$$

and

$$T = t\, t^* \tag{2.10}$$

where * denotes the complex conjugate. When the incident radiation is unpolarized, the transmittance and reflectance are averaged between the two polarizations.

It should be noted that scattering losses on the surfaces can lead to behavior unique to rough samples. For instance, some relations of the Fresnel coefficients, such as $r_{jj'} = -r_{j'j}$ and $1 + r_{jj'} = t_{jj'}$, do not hold for the modified coefficients. Furthermore, the rms roughnesses of the two surfaces of the specimen may differ from each other; in fact, most rough samples used in measurements for this research have a smooth surface and a rough surface. For this reason, turning over the sample causes the rays to strike either the

smooth surface or the rough surface first, resulting in different radiative properties for reflectance. For normal transmittance, this is not the case.

Using scalar scattering theory, certain features are expected in the measured spectra. The energy losses due to surface roughness increase at shorter wavelengths because of the roughness-to-wavelength term in the scattering factor. Two main effects result from this: a reduction in the fringe amplitude toward shorter wavelengths and a decrease in the average transmittance and reflectance in the specular direction toward shorter wavelengths (Montecchi et al., 2001).

To establish the need for using a rough surface approach to modeling thin films, it can be worthwhile to experimentally verify whether the roughness effects on the spectra are significant. One way to do this is to use an instrument equipped for hemispherical measurement, such as a spectrometer with an integrating sphere. Scattering losses need to be considered if the hemispherical spectra values are significantly higher than the corresponding specular spectra values. One could also perform a test involving excluding the specular component of the light incident on the sphere to determine if the diffusely reflected components exhibit maxima and minima (Montecchi et al., 2001).

2.3 Partial Coherence

Scalar scattering theory, discussed in the previous section, is based on a coherent formulation, and in order to accurately model the radiative properties of many thin films with rough surfaces, partial coherence must be considered. Partial coherence, considered alone, has its own characteristic influence on the reflectance and transmittance spectra of

thin films. Before embarking on a discussion of partial coherence, it may be useful to first review the more familiar thin-film optics formulation.

2.3.1. Background

Interference plays an important role in influencing the radiative properties of thin films. When radiation is incident on one of the surfaces of a thin film, partial reflection and transmission at the interfaces lead to multiple reflections within the film. The multiply reflected waves interfere with each other, giving rise to fringes, or interference oscillations, in the spectrum. The amplitudes of the transmitted and reflected electric fields can be summed, resulting in the well-known Airy formulas. This coherent formulation is well-established and can model thin films in certain idealized situations, such as when the surfaces are smooth, parallel, homogeneous, and the optics of the instrument are close to ideal.

One notable effect worth mentioning is the influence of the index of refraction of the thin film on the transmittance. For the case of a slightly absorbing thin layer ($\kappa << n$), the oblique transmittance can be expressed in a compact form as follows (Zhang, 1999):

$$T'_\lambda = \frac{(1-\rho'_\lambda)^2 \tau'_\lambda}{1+\rho'^2_\lambda \tau'^2_\lambda - 2\rho'_\lambda \tau'_\lambda \cos(2\beta)} \tag{2.11}$$

where the phase shift $\beta = 2\pi n_2 \bar{\nu} d \cos(\theta_2)$. Figure 2.2 shows the transmittance plotted against the phase shift, a nondimensional parameter which causes the plot to be independent of thickness. As the index of refraction increases, the minimum value of the fringes gradually decreases until it reaches zero. Increasing the index of refraction no longer changes the transmittance because it is already at zero, the lowest possible value. This shape is critical, and the effect will manifest itself later when the coherence function

is discussed. Further details about the coherent formulation can be found in any radiation or optics reference text and consequently will not be discussed here.

While the wave optics formulas and geometric optics can be applied in a variety of circumstances, treating the partial coherence of the source radiation can be crucial in many practical situations. Indeed, all sources of radiation exhibit some degree of partial coherence. The most chaotic sources of blackbody radiation exhibit coherence to some extent, and even lasers, often regarded as coherent sources of light, have narrow but finite spectral ranges (Mehta, 1963). In determining the optical constants of dielectrics, for instance, using the extreme cases to simplify the situation can lead to significant error (Chen and Tien, 1992; Grossman and McDonald, 1995). "Coherence" in this sense refers to spectral coherence although it can be said the concept of coherent spectral width, discussed later in Section 2.4, addresses both spectral and spatial effects (Grossman and McDonald, 1995).

The present work investigates the common situation that arises when a Michelson interferometer-based spectrometer is used to measure transmittance or reflectance. In this case, the degree of the coherence of the spectrum is reduced by characteristics of the instrument and the sample, such as: angle of incidence, beam divergence, wavenumber interval between data points set by the inherent instrument's resolution, and the surface condition of the sample (Zhang, 1994; 1999). In applying the concepts of partial coherence to FT-IR spectrometry, it is important to distinguish between the two regimes. Perfectly coherent radiation refers to the case when the interference fringes are completely resolved while perfectly incoherent radiation refers to the case when interference fringes are completely unresolved (Zhang et al., 2003). The highest

resolution of the spectrometer for a measurement dictates whether a measured spectrum falls in the coherent or incoherent regimes.

Partial coherence has been treated in many studies of thin films with smooth surfaces. Most of the researchers behind these studies approached the problem by using partial coherence theory. The partial coherence theory of light was developed before 1960 and received considerable attention with the advent of the laser in the 1960s (Born and Wolf, 1975). Applied to thin films, the theory makes it possible to relate the refracted electric fields and multiply-reflected electric fields to arrive at expressions for transmittance and reflectance. These expressions typically contain a term known as the complex degree of coherence, or simply degree of coherence, defined as (Zhang, 1994).

$$\gamma_{jk} = \frac{\left\langle E_j(t) E_k^{*}(t) \right\rangle}{\sqrt{\left\langle E_j(t) E_j^{*}(t) \right\rangle \left\langle E_k(t) E_k^{*}(t) \right\rangle}} \tag{2.12}$$

where E is the electric field, t is time, and the indices j and k refer to different waves. Chen and Tien (1992) and Zhang (1994) used partial coherence theory to predict the radiative properties of thin films with smooth surfaces and layered structures. Grossman and McDonald (1995) introduced a wavenumber-dependent degree of coherence in a study of the partial coherence of dielectric lamellae with smooth surfaces and emphasized the importance of instrumental factors and the wavenumber-dependent partial coherence. In modeling the transmittance and reflectance of polycrystalline CVD diamond layers with roughnesses of less than 100 nm, Petrich and Stenzel (1994) considered the coherence disturbance of light incident on the rough surfaces. They integrated the transmission and reflection coefficients over the rms film thickness based on a Gaussian

distribution but did not consider the instrumentation effects such as resolution or beam divergence.

In quantifying the effect of partial coherence on the radiative properties, various parameters can be defined. First, the free spectral range $\Delta\bar{\nu}$ (where $\bar{\nu}$ is the wavenumber in cm^{-1}) is the separation between two interference maxima (or minima), and it can be shown that $\Delta\bar{\nu} = (2n_2 d\cos\theta_2)^{-1}$. It should be noted that throughout this thesis, wavenumber is used for the units of the spectra, which causes the free spectral range to be independent of wavenumber when the layer is nondispersive. The conversion between wavenumber (cm^{-1}) and wavelength (μm) is as follows: $\bar{\nu} = 10000/\lambda$. Figure 2.3, which includes the mid-IR spectral region (500 – 5000 cm^{-1}) that is studied in this work, is intended to help illustrate this relationship. When differential quantities arise, the following expression can be applied: $\bar{\nu}d\bar{\nu} = \lambda d\lambda$. The free spectral range in wavelength is therefore wavelength-dependent: $\Delta\lambda = \Delta\bar{\nu}/\lambda^2$.

Furthermore, to describe the amplitude of the transmittance fringes, it is useful to define the fringe contrast as

$$\Phi = \frac{T_{\max} - T_{\min}}{T_{\max} + T_{\min}} \tag{2.13}$$

Although the resolution of the instrument is defined as the smallest interval that the instrument can resolve two narrow band spectral peaks (Griffiths, 1986), the resolution specified by the instrument may be considered as the wavenumber interval over which the instrument integrates the spectrum at any given point. In most commercially available FT-IR spectrometers, the wavenumber spacing between two consecutive data points is equal to half the resolution specified by the instrument.

The actual resolution of the instrument depends on several factors, including aperture size and the collimation of the beam. Aside from the beam divergence, the sample thickness may vary due to non-parallelism or roughness over the beam spot size on the sample, causing the phase angle $\beta = 2\pi d n_2 \cos\theta_2 / \lambda$ to fluctuate, reducing the coherence of the beam. The effective resolution of the measurement also depends on the instrument and the free spectral range of the samples. For example, if the resolution of the instrument is much smaller than the free spectral range of the sample, its effect on the measured spectra may be negligible. The effects of non-parallelism and surface roughness on the degree of coherence can generally be neglected when the thickness variation is less than one-tenth of the wavelength in the medium.

2.3.2 Spectral Averaging

Partial coherence theory is one method of treating partial coherence in thin films. However, Chen and Tien (1992) showed that partial coherence theory predicts the same results as spectral averaging of the transmittance or reflectance spectra calculated from the coherent formula over a finite wavenumber interval. Nevertheless, they do not appear to have explored this alternative approach in-depth. Spectral averaging is often called fringe smoothing because the fringe contrast is reduced and the curve becomes smoother, a direct result of the integration operation. Fringe smoothing involves averaging over the data points within a certain wavenumber interval using the following integration expression:

$$\overline{T}(\overline{\nu}) = \frac{1}{\delta\overline{\nu}} \int_{\overline{\nu}-\delta\overline{\nu}/2}^{\overline{\nu}+\delta\overline{\nu}/2} T(\overline{\nu}) d\overline{\nu} \qquad (2.14)$$

where $\delta\bar{\nu}$ is the wavenumber interval over which the transmittance values are averaged. This is repeated to obtain a curve of averaged data points. The wavenumber interval used for averaging, which is akin to an "effective" spectral resolution, can be referred to as the coherent spectral width and is itself a function of wavenumber in the present work.

Figure 2.4 shows the results of fringe smoothing on a typical transmittance spectrum (d = 25 μm) using various coherent spectral widths. As $\delta\bar{\nu}$ increases from the nonsmoothed case (0 cm^{-1}) to 50 cm^{-1} and then to 80 cm^{-1}, the fringe contrast decreases. When the coherent spectral width equals the free spectral range, the fringes disappear, and the incoherent case results. As the coherent spectral width increases above the free spectral range, however, the peaks and valleys of the fringes become inverted.

Spectral averaging has some advantages over using partial coherence theory. The coherent spectral width can be compared with the instrumental specified resolution, and conclusions can be drawn about the effects of instrumental averaging. Although partial coherence theory, based on a rigorous electromagnetic formulation, provides a direct solution for the radiative properties, integrating over data points can in some cases be easier to apply than the equations from partial coherence theory. Both methods require numerical evaluation.

2.3.3 Coherence Function

In order to quantify the effect of fringe smoothing and relate that to the coherence of the radiation, this work introduces the coherence function, which is defined as follows:

$$\phi = \frac{T(\bar{\nu}_{\max}) - T(\bar{\nu}_{\min})}{T_{coh}(\bar{\nu}_{\max}) - T_{coh}(\bar{\nu}_{\min})} \tag{2.15}$$

The denominator equals the maximum coherent transmittance minus the minimum coherent transmittance, and the numerator equals the difference in transmittance at these same wavenumbers. Figure 2.5 illustrates this definition. After substituting for the smoothing terms in the numerator, the expression becomes:

$$\phi = \frac{\frac{1}{\delta\bar{\nu}} \int_{\bar{\nu}_{max}-\delta\bar{\nu}/2}^{\bar{\nu}_{max}+\delta\bar{\nu}/2} T(\bar{\nu}) d\bar{\nu} - \frac{1}{\delta\bar{\nu}} \int_{\bar{\nu}_{min}-\delta\bar{\nu}/2}^{\bar{\nu}_{min}+\delta\bar{\nu}/2} T(\bar{\nu}) d\bar{\nu}}{T_{coh}(\bar{\nu}_{max}) - T_{coh}(\bar{\nu}_{min})} \tag{2.16}$$

The coherence function has two important applications. First, it quantifies the reduction in the fringe contrast resulting from fringe smoothing. In the perfectly coherent case, ϕ equals one. The coherence function becomes zero for the incoherent case. Although the coherence function is similar to the fringe contrast, the sign of the coherence function also gives information about the fringe flipping effect. Second, the coherence function provides insight into the coherent spectral width needed for fringe flipping to occur. Where the value of the coherence function is negative, the peaks and troughs are inverted. By relying on the fringe contrast, the coherence function is in some sense more intuitive than the degree of coherence defined in Eq. (2.12). Because it provides information about the coherence or incoherence of the radiation, the coherence function can help determine which approach (thin-film optics, a partial coherence method, or geometric optics) is most suitable for modeling the radiative properties for a particular case.

In Figure 2.6, the coherence function is plotted versus a nondimensional parameter assuming a thickness of 500 μm using a range of indices of refraction (neglecting absorption) that includes 3.42, the approximate refraction index of silicon at a wavelength of 1500 cm^{-1}. The nondimensional parameter is the coherent spectral width divided by the free spectral range. As the index of refraction increases above six or seven,

the peaks and troughs of the coherence function begin to flatten and a dip begins to form where $\delta\bar{\nu}$ is between zero and one. This unusual behavior is probably a result of the effect described in Section 2.1 that appears when the minima of the coherent transmittance gradually decreases with increasing refractive index and eventually bottoms out at zero. This plot is independent of thickness, and although varying the thickness did produce slight changes in ϕ, the effect was attributed to numerical error. The result is expected since the coherent spectral width used for fringe smoothing is proportional to the free spectral range, and the thickness effect on ϕ is thus eliminated. As expected, the locations where ϕ equals zero corresponds to multiples of the free spectral range (where the x-axis values are integers) since in these instances the spectra become completely smoothed.

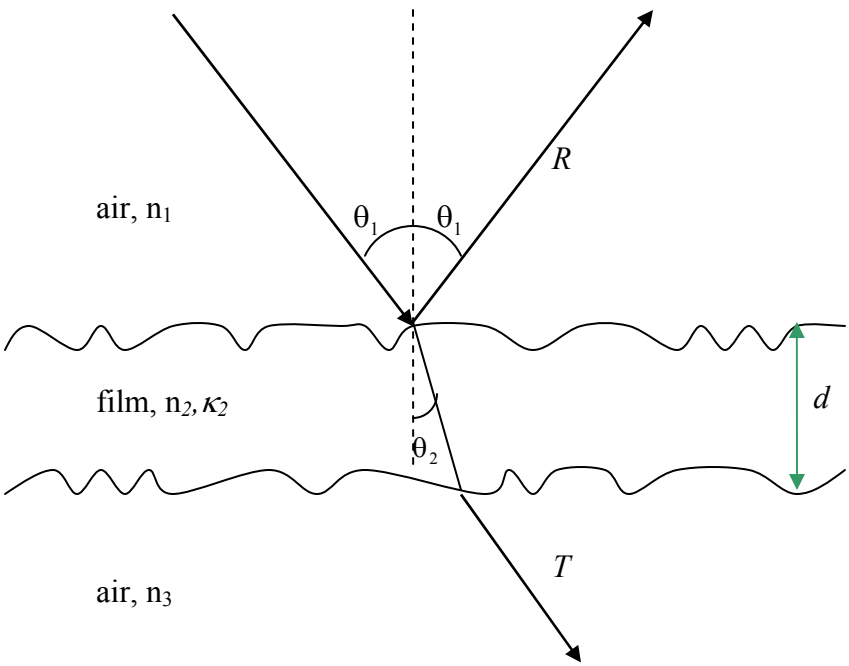

Figure 2.1: Illustration of the transmittance and reflectance of a thin film with rough surfaces.

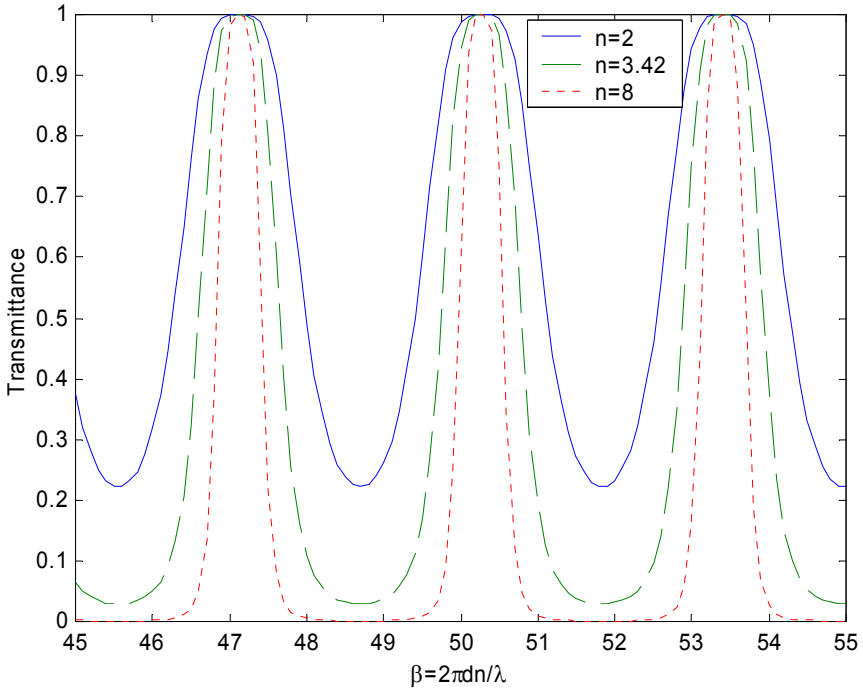

Figure 2.2: Coherent transmittance (normal incidence, $n = 3.42$, $d = 15$ μm) versus phase shift.

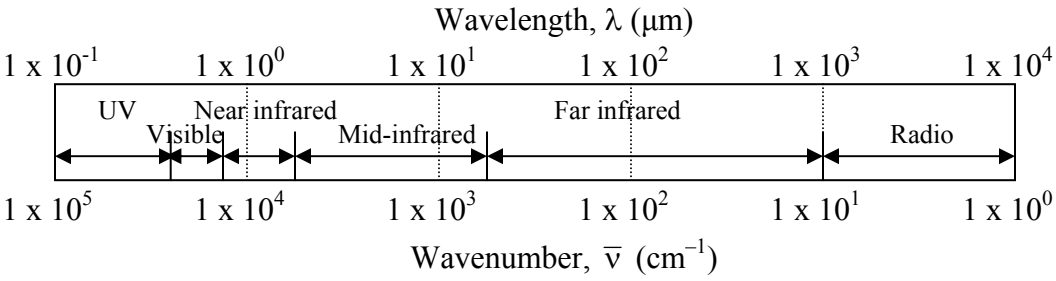

Figure 2.3: Spectrum of electromagnetic radiation.

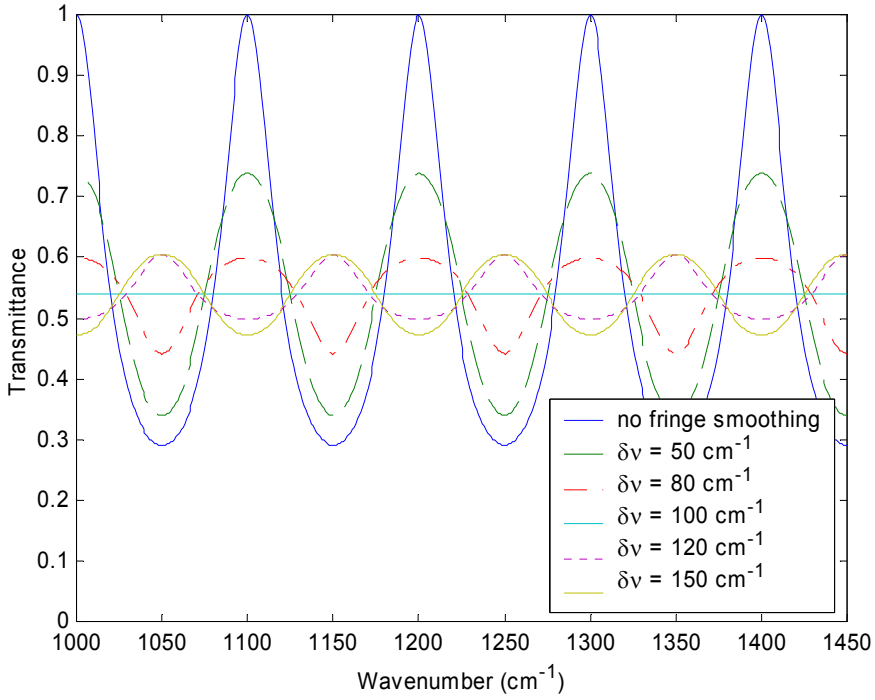

Figure 2.4: Illustration of fringe smoothing using several coherent spectral widths.

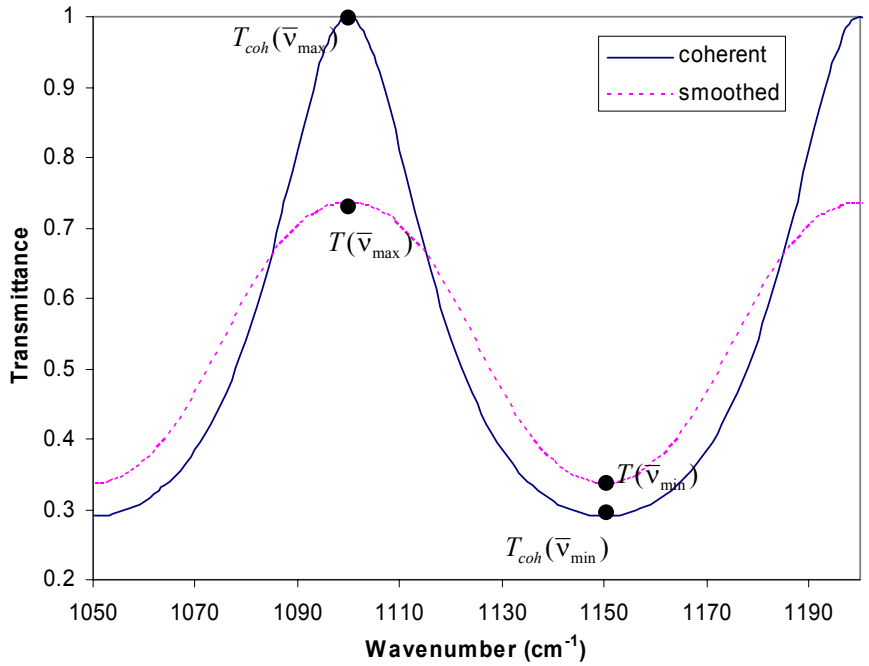

Figure 2.5: Illustration of coherence function definition.

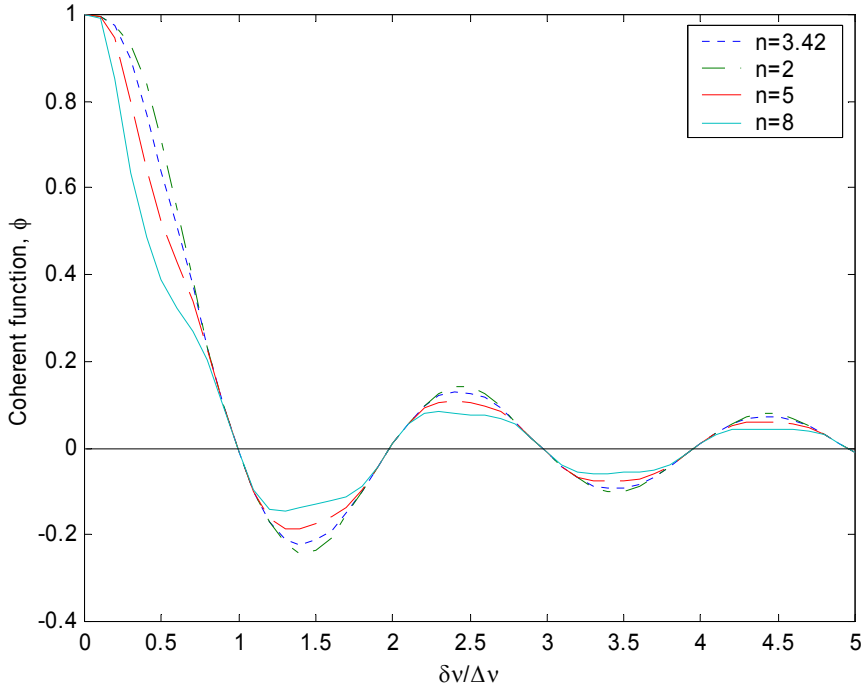

Figure 2.6: Coherence function versus the ratio of the coherent spectral width to the free spectral range.

CHAPTER 3

MEASUREMENTS

3.1 Theory of Fourier-Transform Spectrometry

Fourier-transform infrared (FT-IR) spectrometry, the technique used for obtaining transmittance and reflectance measurements in this work, has become one of the most widely used methods for acquiring spectra in the infrared. The applications in science and industry are extensive and range from chemical analysis to measurements of radiative properties. Fourier-transform spectrometers, the general class of instruments, obtain spectra (in many cases beyond the infrared) by collecting an interferogram using an interferometer, digitizing the signal, and then performing an inverse Fourier transform to obtain the spectrum. An important advantage of FT-IR systems is that they can be used as integrated tools for temperature measurement or the determination of film thickness, surface roughness, dopant concentration, or impurities (Zhang, 2000).

The origins of Fourier-transform interferometry date back to 1880, when the American physicist Albert A. Michelson used the interferometer to measure the velocity of light, an achievement for which he subsequently won the Nobel Prize. In the 1950s and 1960s, developments in astronomy and atmospheric science together with the advent of the Cooley-Tukey algorithm, which significantly reduced the computation time of Fourier transforms, propelled Fourier-transform spectroscopy into greater prominence and usage. Today, the method is widely used for routine analysis of the transmittance and reflectance of solid samples.

Radiation in a Fourier-transform spectrometer originates at a broadband source and proceeds through several stages until the spectrum is calculated, as shown in Figure

3.1. First, light that leaves the source is collimated before reaching the Michelson interferometer. The Michelson interferometer is an important part of the Fourier-transform spectrometer because it produces a signal known as the interferogram. The interferogram, which results from the interference of waves contained in the beam that reaches the detector, is related to the spectrum via a mathematical operation, the Fourier transform. In a sense, all of the information about the spectrum is gathered at the same time and is sorted out later using the Fourier transform.

The Michelson interferometer divides a beam of radiation into two components and recombines them after introducing a path difference. Figure 3.2 shows the basic design, which consists of a beam splitter, a fixed mirror, and a moving mirror. The beam splitter transmits half the incident radiation and reflects the other half. The transmitted beam passes to a moveable mirror while the reflected beam continues on to a stationary mirror. Both beams recombine when they return to the beam splitter, with one part passing to the detector and the other part to the source. Hence, as the moveable mirror changes position, the radiation at the output produces the interferogram signal. Although most FT-IR spectrometers are based on the Michelson interferometer, it is interesting to note that a Fourier-transform instrument incorporating a Wollaston polarized prism, which lacks a moving mirror, has been adapted for radiation thermometry and is only about the size of a human fist (Dunmore and Hanssen, 1998).

The interferogram is often a graph of electrical signal as a function of the optical path difference (OPD), δ, which is commonly referred to as the retardation. To qualitatively understand how an interferogram is related to a corresponding spectrum, one can consider an idealized situation in which the radiation source is monochromatic. At

zero path difference, the beams from the fixed and moveable mirrors are perfectly in phase and the beams interfere constructively. As the moveable mirror is displaced, the beams become more out of phase and interfere destructively on recombination. Further displacement of the moveable mirror can again lead to constructive interference, resulting in the sinusoidal behavior of the interferogram, as shown in Figure 3.3 (a). For monochromatic radiation, the interferogram equation is as follows:

$$I_d = E(t) \cdot E(t)^* = \frac{1}{4} E_0^2 \cdot 2[1 + \cos(\frac{2\pi}{\lambda} \cdot 2\delta)] = \frac{1}{2} E_0^2 [1 + \cos(2\pi \cdot 2ut \cdot \bar{\nu})] \qquad (3.1)$$

where E is the electric field, I_d is the interferogram, u is the velocity of the moving mirror, t is time, and $\bar{\nu}$ is wavenumber. The electric field E is given by

$$E(t) = \left(\frac{1}{2} E_0 e^{ik2x_0} + \frac{1}{2} E_0 e^{ik(2x_0 + 2\delta)} \right) e^{-i\omega t} \qquad (3.2)$$

Interferogram values repeat themselves at regular intervals of retardation for line sources with simple spectra. For a spectrum containing only two closely spaced spectral lines, for instance, as shown in Figure 3.3 (b), an envelope function appears in the interferogram and has a width dependent on the beat frequency, or difference between the two frequencies of the doublet. A small frequency difference leads to a large envelope function. From this, it may be easier to understand why the resolution limit, or highest possible resolution of the spectrum, equals the inverse of the largest achievable optical path difference, which leads to the high resolution capability of FT-IR spectrometers. When the source is broadband, the interferogram becomes a complex looking oscillatory signal with a maximum at zero path difference and secondary peaks at other positions. Figure 3.3 (c) shows a typical background interferogram and broadband spectrum, as obtained from the spectrometer used in the measurements. As the mirror moves away

from zero path difference, the phases of the two beams never again return to the situation of perfectly constructive interference.

To obtain the transmittance spectrum of a material, radiation that leaves the Michelson interferometer passes through the sample onto the detector. a typical transmittance or reflectance spectrum is obtained by measuring the signal without the sample and once more with the sample. For this reason, FT-IR systems are classified as single beam spectrometers (Bell, 1972). The analog interferogram signal is then digitized, and the Fourier transform operation is performed entirely in software to yield the spectrum. Mathematically, the interferogram, I, is related to the spectrum, B, by the cosine Fourier transform.

$$I(\delta) = \int_{-\infty}^{\infty} B(\bar{\nu}) \cos(2\pi\bar{\nu}\delta) d\bar{\nu} \tag{3.3}$$

The voltage spectrum can be determined from the interferogram by taking its inverse cosine Fourier transform as follows:

$$B(\bar{\nu}) = \int_{-\infty}^{\infty} I(\delta) \cos(2\pi\bar{\nu}\delta) d\delta \tag{3.4}$$

It is important to note that some scientific circles use a slightly modified form based on a different mathematical definition of the Fourier transform.

The inverse Fourier transform is computed using the fast Fourier transform (FFT) algorithm. Instrumental imperfections and inherent limitations, however, need to be accommodated by performing phase correction and apodization. If during sampling, a measurement of a data point at zero path difference is not taken at the intended true origin, problems can arise in the computed spectrum. For instance, a phase shift, β, can be introduced into the interferogram expression as follows:

$$I_d = \frac{1}{2} E_0^2 [1 + \cos(2\pi \cdot 2ut \cdot \bar{\nu} + \beta)] \tag{3.5}$$

The process of apodization involves multiplying the interferogram by a weighting function so that the intensity falls smoothly to zero at the ends. This is necessary because the moving arm of the interferometer only moves a finite distance, resulting in an abrupt truncation of the interferogram when the moving mirror stops. This creates lobes near the ends of the interferogram. Every apodization function has a corresponding instrument line shape (ILS) in the frequency domain. Usually, apodization functions with instrument line shapes that have low full width at half max (FWHM) values and have small secondary peaks with respect to the highest peak are most desirable. On the other hand, their principle disadvantage is that they can degrade the resolution. Triangular, cosine, and boxcar functions are commonly used in commercial software.

FT-IR spectrometers differ from conventional dispersive spectrometers in fundamental ways. Dispersive spectrometers spatially separate the individual frequencies of the radiation one resolution element at a time as the light passes through a sample. This can be accomplished by the use of a prism or a diffraction grating. FT-IR instruments, on the other hand, modulate the different frequencies and use a Fourier transform to separate them. Multiplex (Fellgett) advantage refers to the fact that all the wavenumbers are observed simultaneously in FT-IR spectrometry. In addition, if spectra are acquired under identical conditions (same resolution, measurement time, throughput, optical efficiency), FT-IR spectrometers yield a higher signal-to-noise ratio than dispersive spectrometers. It is higher by a factor of the square root of the number of resolution elements (Griffiths and de Hasseth, 1986). Relatively fast scan rates (often less than a few minutes over the mid-IR range) are also possible.

FT-IR spectrometers also offer high throughput since they do not require slits like grating spectrometers. Jacquinot originally expressed the ability to collect large amounts of energy at high resolution as a throughput, or *une étendue*. Throughput, E, is defined as

$$E = dA \cdot d\Omega \tag{3.6}$$

where dA is the projected area of the collimator and $d\Omega$ is the solid angle from the point source to the detector element. The high throughput that is achievable is described by the Jacquinot advantage (Griffiths and de Hasseth, 1986). It can be shown that for the same area and resolving power, the ratio between interferometer throughput to grating throughput can be large, leading to comparatively high optical efficiency for FT-IR for a given source area (Bell, 1972).

Another important characteristic of FT-IR spectrometry is the absence of stray light. However, because the interferometer modulates the light from the spectrometer's light source, stray unmodulated radiation does not cause error in the transmittance values. High wavenumber accuracy also follows from the Fellgett and Jacquinot advantages and is a consequence of the accurate movement of the moving arm, which yields a precise interference pattern (Bell, 1972).

3.2 Instrumentation Issues

Despite the advantages in terms of measurement speed and spectral (abscissa-scale) accuracy, FT-IR spectrometry has some drawbacks. Measurements can be prone to instrumental effects, such as interreflection error, detector nonlinearity and non-equivalence, and background thermal radiation (Kaplan et al., 1997). In some cases, the

same optical design elements responsible for the superior performance lead to severe error. For these reasons, Kaplan and Hanssen (1998) noted that their FT-IR measurements of transmittance and reflectance were usually to within 0.2 to 1 percent relative uncertainty, depending on sample and measurement type. In addition, the spatial resolution is limited by diffraction, which is on the order of a wavelength (Zhang, 2000). Although it can take less than a second for one scan to occur over the mid-IR region, multiple scans are routinely collected and averaged to obtain a better signal-to-noise ratio.

Sources of radiometric (ordinate-scale) error in particular have been the focus of extensive theoretical and experimental studies over the past decade. Flik and Zhang (1992), for instance, showed that high power incident on the detector, either from the source or from a heated sample, can give rise to nonequivalent detector responsivity. The mechanism for this type of error is that the sample-spectrum responsivity differs from the background-spectrum responsivity. These effects need to be considered if the high incident radiation power is not sufficiently attenuated or the detector temperature is transient.

The beam geometry can also dramatically affect FT-IR measurements. Beam divergence changes the degree of collimation of the beam and occurs throughout the spectrometer. This happens, for instance, when the beam passes through the sample. The interferometer output beam forms a cone of light with the sample holder, as shown in Figure 3.4. The numerical aperture, or *f-number* (often written as *f/#*), is defined as $f/\# = f/D$, where f is the focal length, and D is the diameter of the aperture (Born and Wolf, 1975). Increasing the *f-number* creates a more collimated beam, increasing the spatial

resolution of the instrument. Ideally, the solid angle should be as small as possible without compromising throughput. Although the conical geometry is set by the manufacturer, this effect can be studied using aperture stops placed over the output beam cover. Kaplan et al. (1997), in their study of radiometric accuracy, calculated the transmittance of a typical beam for an FT-IR spectrometer to be on the order of 0.05 percent to 0.2 percent lower than the collimated normal incident value, based on a comparison with laser measurements. The difference, they noted, generally increased with shorter wavelengths and thicker samples. While these effects may seem small, modifying the spatial resolution can drastically impact the fringe contrast for partially coherent spectra, a consequence that is easily observable.

In a preliminary appraisal of the sources of systematic error in the FT-IR spectrometer, that is, random or unexpected error associated with the implementation or interpretation of the Fourier transform process used in acquiring the spectra, Birch and Clarke (1998) noted that interreflection error may be particularly troublesome; it can be significant, yet difficult to quantify and correct for. They identified seven categories in which interreflection can occur, either between surfaces in the instrument or the sample surfaces. Depending on the relative phase differences, interreflections can cause an increase, decrease, or no change in the spectral output (Birch and Clarke, 1998). Kaplan and Hanssen (1999) also analyzed interreflection error by placing blocks made of IR-absorbing black felt between the sample and the detector and between the sample and the source. They assigned an error of 0.2 percent to 0.4 percent relative uncertainty due to interreflections from metallic samples–a comparatively large source of error. Kaplan et al. (1997) recommended the following steps to reduce interreflection error:

1) Tilt the sample.

2) Tilt the detector.

3) Use low-reflectance detectors, such as windowless black-coated detectors.

4) Use an attenuator, such as a neutral density filter.

5) Use a half-beam block, as previously described.

Gaseous absorption is a common occurrence in spectroscopic measurements, which can be addressed with purging. Without purging, absorption lines at frequencies corresponding to the vibrational and rotational transitions modes of the water vapor and carbon dioxide molecules are apparent in the mid-IR range. By purging, N_2 gas displaces the water vapor and carbon dioxide in the air of the source chamber, the output cover, the detector cover, and the area surrounding the sample holder. Figure 3.5 shows the effect of purging the spectrometer after approximately 40 min at a tank output pressure of about 2 psi. From this, it is clear that purging significantly reduces the carbon dioxide absorption in addition to the water vapor absorption near 5500 cm^{-1}. In most of our measurements, however, the desired features that we sought in our spectra did not require purging.

Aside from these issues, which commonly plague measurements obtained using Fourier-transform spectroscopy, the scattering properties of the sample are of particular importance in the present study since they can render measurement results inaccurate or easily misinterpreted (Hanssen and Kaplan, 1998). Specific problems are posed by scattering at the sample surfaces or in the volume of the sample. Channeling effects can cause light to exit at or near the sample's edges, which can be influenced by how the sample is mounted and its orientation and geometry. This can compromise the accuracy of the transmittance and reflectance measurement since the spectrometer may not be

equipped to account for the scattered light and even with hemispherical measurement systems, not all of the light can necessarily be measured.

3.3 FT-IR Spectrometer Description

The instrument used to obtain data for this work was the FTLA2000 series (MB154S) spectrometer manufactured by ABB Bomem, the interior of which is shown in Figure 3.1. Rather than using a stationary and moveable mirror, this spectrometer employs a cube-corner design with two moveable mirrors, which allows for permanent alignment. A He-Ne laser measures the position of the mirrors using the interferometer fringes from the laser's monochromatic light. The instrument has a wavenumber range of 12,000 cm^{-1} to 500 cm^{-1} and a maximum resolution of 1 cm^{-1}. The default *f-number* of the output beam diameter to the sample is 5.6 and the maximum beam divergence is 11.3 deg. The spectrometer uses a ceramic globar mid-IR source and a deuterated triglycine sulfate (DTGS) pyroelectric detector. The opening on the sample holder, which is 6 mm in diameter, limited the beam spot size on the sample. Spectra were measured at room temperature in the wavenumber range from 5000 cm^{-1} to 500 cm^{-1} ($2\ \mu m \le \lambda \le 20\ \mu m$). For the measurements, the cosine truncation function was used for the apodization function. Each spectrum was averaged over 16 scans. For reflectance measurements, the spectrometer was outfitted with a 10-deg specular reflectance accessory, as shown in Figure 3.6. Because the gold mirror used for the background spectrum measurements has a reflectance of about 99 percent, all measured reflectance values in this study were increased by one percent.

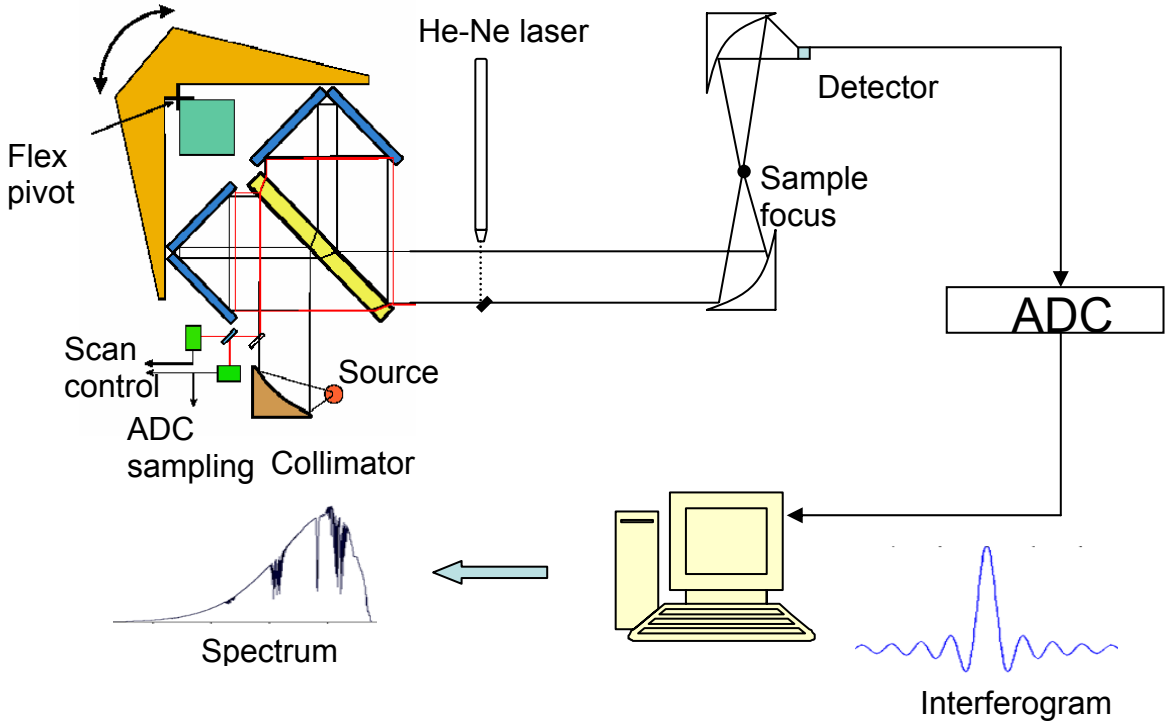

Figure 3.1: Schematic of ABB Bomem FT-IR spectrometer.

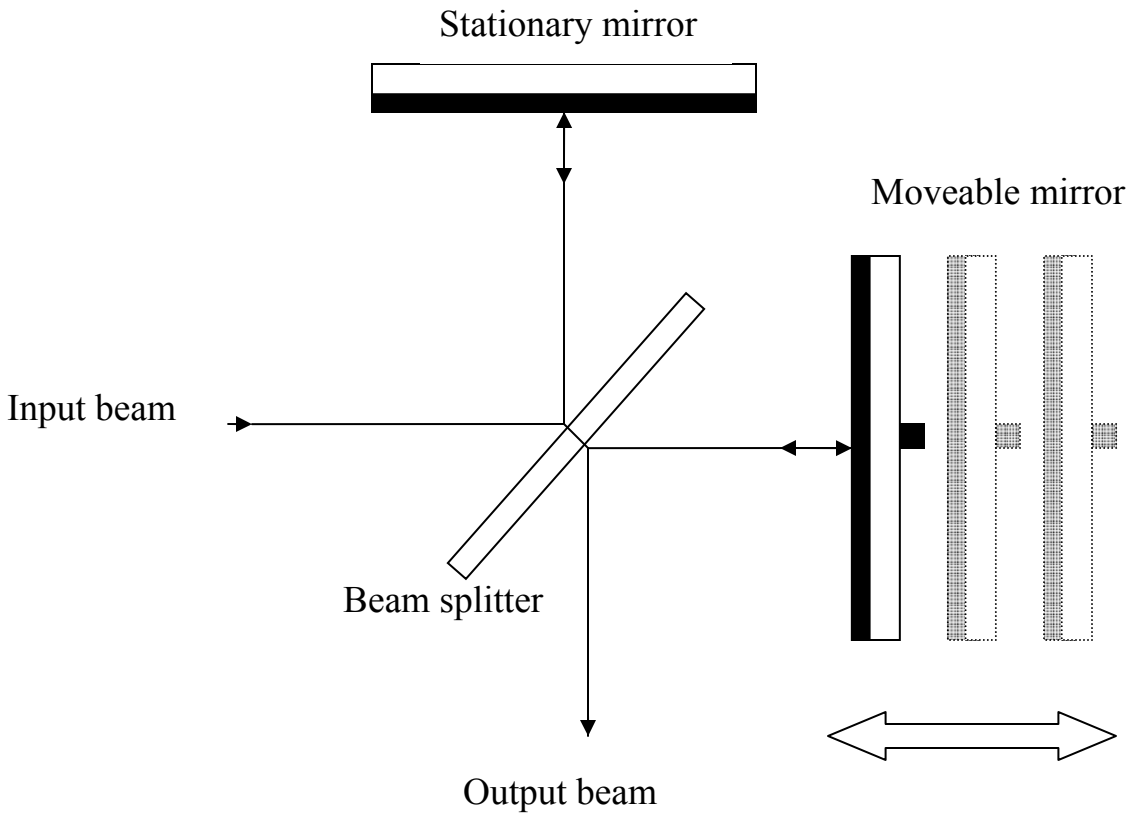

Figure 3.2: Schematic of Michelson interferometer.

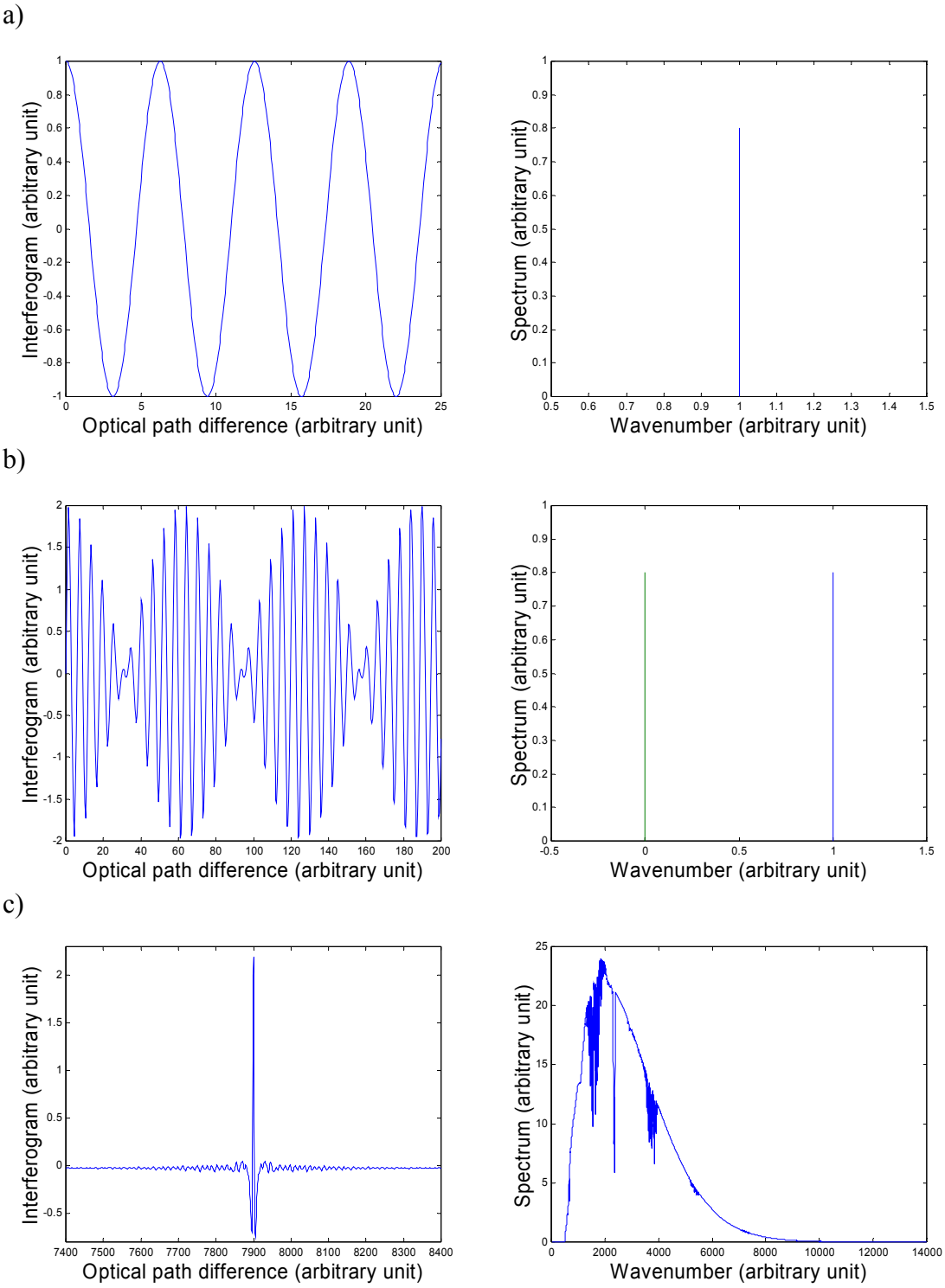

Figure 3.3: Typical interferograms and corresponding spectra: a) monochromatic; b) two frequencies; c) broadband.

(a)

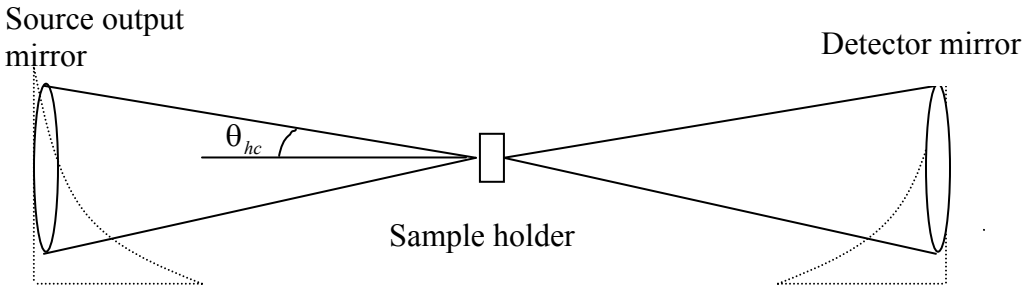

(b)

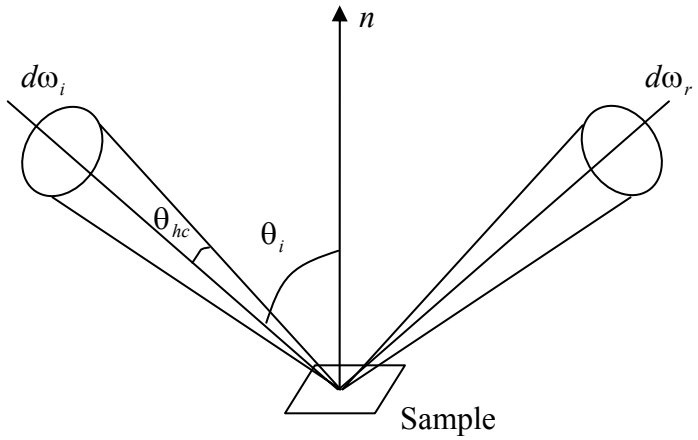

Figure 3.4: Illustration of conical radiative properties: a) transmittance; b) reflectance.

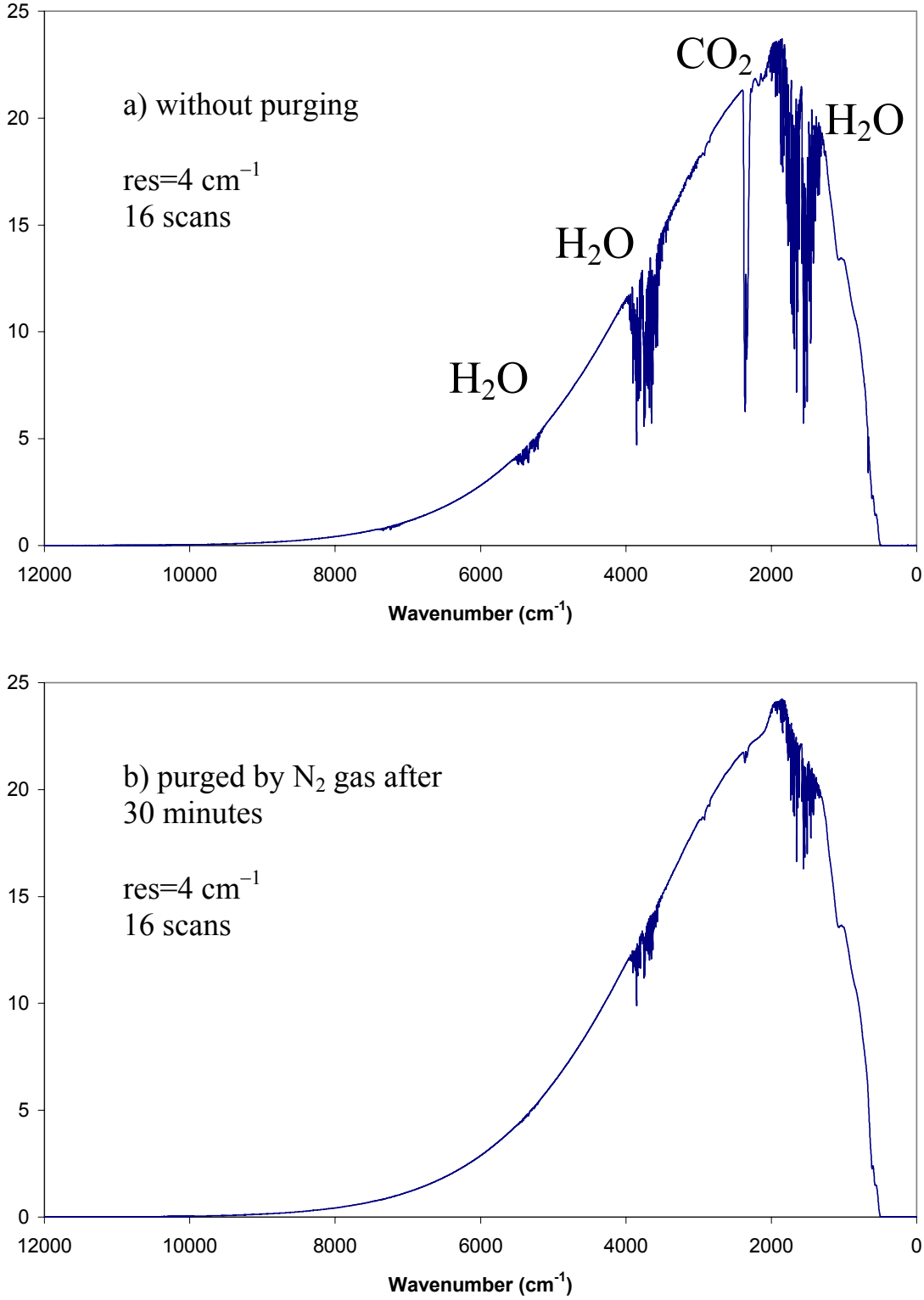

Figure 3.5: Effect of gas purging: a) unpurged background spectrum; b) purged after 30 minutes.

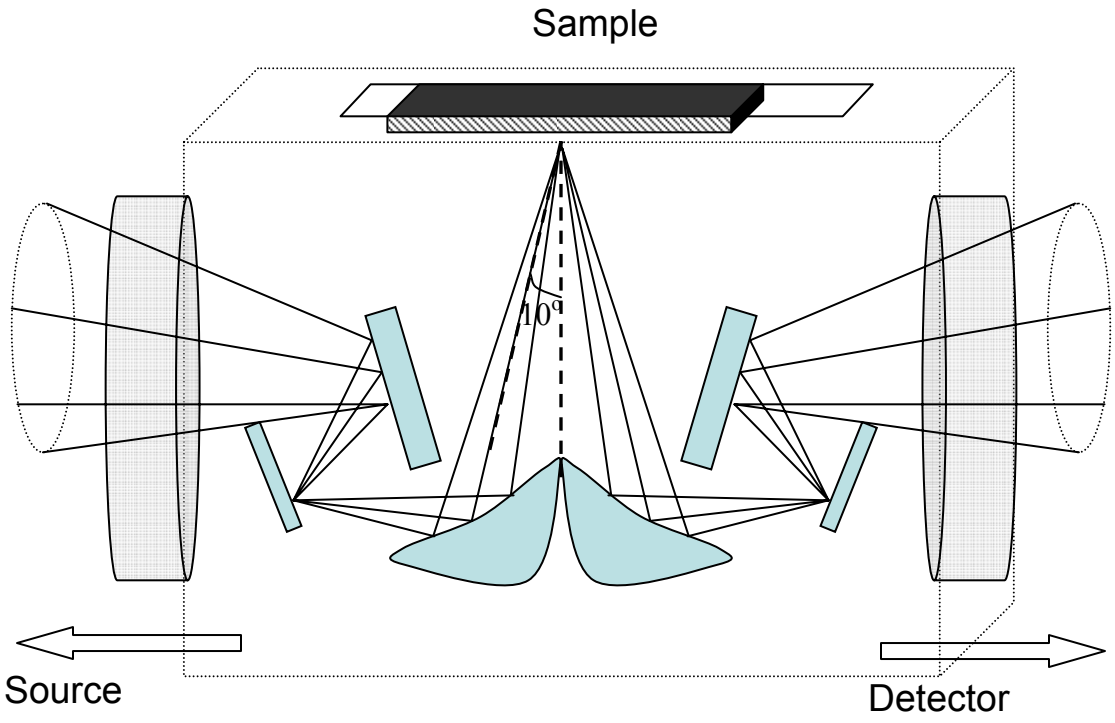

Figure 3.6: Diagram of reflectance accessory.

CHAPTER 4

RESULTS AND DISCUSSION

4.1 Sample Descriptions

Using the FT-IR spectrometer, measurements of several samples of silicon and CVD diamond film were obtained in the mid-infrared spectral region (500 to 5000 cm^{-1}). Table 4.1 summarizes the sample characteristics and includes the labeling scheme adopted in this study. Silicon is a readily available semiconductor material whose optical constants in the infrared have been well studied and tabulated (Edwards, 1985). The silicon wafers were single-crystal with <100> orientations and ranged from pure to highly-doped. A CVD diamond thin film was also used to study the effects of surface roughness. The diamond film was formed on a smooth substrate, and then the substrate was etched away, leaving a smooth surface on one side while the other side was left unpolished. CVD diamond films form polycrystalline layers when grown on nondiamond substrates, and the polycrystalline layers give rise to optical scatter in the interior of the layer. A deposition process minimizing the amount of wasted flowing feed gas was used for creating the sample used in this study (Farabaugh et al., 1995). Deposition parameters, such as temperature and deposition rate, play critical roles in determining the structural and optical properties of CVD diamond film, and more detailed discussions can be found in the literature (Robins et al., 1991).

To better understand the effects of surface roughness, surface statistics were determined from topographic data using an atomic force microscope (AFM) and a surface profilometer. The AFM works by using a cantilever tip, which experiences a repulsive force due to the overlap of electron clouds when brought close to a surface (Zhang et al.,

2003). This gives the surface morphology, represented as an image while the profilometer uses a vertically positioned stylus to probe the surface mechanically and consequently gives a cross-sectional profile of a given sample. The profilometer has a diamond tip 2 - 3 μm in diameter, which sets the lateral resolution, and a 60-deg conical angle. Three silicon samples were measured with the profilometer, as summarized in Table 4.2, and the AFM was used for a silicon sample and the diamond film sample. To supplement the profilometer data, photographs were also taken using an optical microscope. The AFM system provided image statistics, such as root-mean-square (rms) and mean surface roughness while the profilometer provided height information. From this height data, the rms optical roughness, σ_{rms}, was determined using the following expression:

$$\sigma_{rms} = \sqrt{\frac{1}{L}\int_0^L [h(x) - \bar{h}(x)]^2 \, dx} \tag{4.1}$$

where L is the total sampling length, h is the height and x is the horizontal coordinate. The autocorrelation length, τ, is the value of the translation length at which the autocorrelation function drops to 1/e of its peak value. This can be defined as follows:

$$\int_0^{\tau} h(x)h(x+\tau)dx = \frac{1}{e}\int_0^{\tau} [h(x)]^2 \, dx \tag{4.2}$$

It should be noted that these statistical descriptors are most suitable for surfaces that vary in only one direction, but similar expressions for 2-D surface topographies also exist (Mahan, 2002). Conclusions from these calculations and measurements are drawn in Section 4.3 for each sample measured.

4.2 Double-Side Polished Samples

In order to focus on the effects of partial coherence independently of surface roughness, thin double-side polished samples were needed, and samples D1, D2, and D3 satisfied this requirement. The transmittance of samples D1 and D2 was measured with a spectral resolution of 1 cm^{-1} (the highest resolution of the instrument). The same resolution was used for measuring the reflectance of sample D3.

In order to calculate the specular transmittance and reflectance, Eq. (2.10) was used along with tabulated optical constants of silicon for the mid-IR range, taken from Palik's handbook (Edwards, 1985). Applying scalar scattering theory is unnecessary since the scattering factors in Eqs. (2.7) and (2.8) are equal to unity. The thickness of the sample was taken as an adjustable parameter to fit the free spectral range $\Delta\bar{\nu} = (2n_2 d)^{-1}$ and the fringe locations. The rms roughness of the rough surface was determined by matching the mean value of the transmittance. Volume scattering and inhomogeneities in the optical properties of the samples are neglected in the present study because it is expected that for the samples used, the effects of surface scatter are dominant.

Because the degree of coherence generally decreases with increasing wavelength, the coherent spectral width used for spectral averaging is wavenumber-dependent in the present work. The relationship is based on assumptions resulting from the coherent formulation and the belief that instrumental effects, which also contribute to the degree of coherence, are negligible. Upon traversing the film, the phase shift of the electric field, defined by $\beta = 2\pi\bar{\nu} n_2 d\cos\theta_2$, depends on the product of $\bar{\nu}d$ if the change in n_2 is neglected. Therefore, for the same thickness variation, the phase shift varies linearly with

wavenumber. The phase shift is also assumed to have a linear relationship with the coherent spectral width in the partial coherence regime. Based on these assumptions, fringe smoothing was conducted by varying the coherent spectral width linearly with the wavenumber in the spectral integration: $\delta\bar{\nu} = a\bar{\nu} + b$, where a and b are constants. In contrast, Grossman and McDonald (1995) considered the beam divergence and arrived at a quadratic, rather than linear, relationship between the degree of coherence and wavenumber. Table 4.3 summarizes the constants used for achieving the best fits presented in this section.

The fitting procedure used in this study represents a semiempirical method for modeling the transmittance and reflectance. By matching the fringe locations, and assuming the optical constant data are applicable to the sample, the thickness can be determined by trial-and-error. In some cases, the thicknesses were measured using the micrometer. Fitting the magnitude of the transmittance requires spectral averaging by integration over a coherent spectral width $\delta\bar{\nu}$. If the wavenumber range of the transmittance or reflectance spectrum being considered is sufficiently narrow, the value of the coherent spectral width for spectral averaging can be approximated as constant. However, as mentioned earlier, $\delta\bar{\nu}$ generally depends on the wavenumber range of consideration.

The measured and predicted normal transmittance of sample D1 are plotted in Figure 4.1 (a). The measurement was conducted with the spectrometer set to a resolution of 1 cm^{-1}, and the free spectral range of the silicon is approximately 41.3 cm^{-1}, which varies slightly in the wavenumber region of 500 cm^{-1} to 5000 cm^{-1} due to the dispersion of silicon. Assuming that accurate indices of refraction were used, the thickness of the

silicon wafer was determined to be 35.4 μm from curve fitting, which differs 1.2 percent from the nominal thickness of 35 μm. Using the micrometer, the thickness was determined to be 33.9 ± 3.9 μm. Before spectral averaging, the measured transmittance clearly has a much smaller fringe contrast compared to that predicted by thin-film optics. A coherent spectral width equal to 9.91 cm^{-1} (at 1000 cm^{-1}) was needed for fitting, and this value is quite different from the resolution of the instrument. This suggests that beam divergence, which contributes to partial coherence along with instrumental averaging, may have significantly reduced the fringe contrast of the transmittance. Nonparallelism of the thin film surfaces should lead to similar behavior, but it is assumed that the effect is less significant than the beam divergence. The excellent agreement achieved indicates that sample D1 possesses characteristics suitable for thin-film optics.

For the case of the transmittance of sample D2, shown in Figure 4.2, the best fit achieved required additional considerations. Using a single thickness value and the tabulated data of the optical constants, it was not possible to match the fringes over the entire wavelength range studied. Figure 4.2 (a) shows the good agreement in the wavenumber region from 1460 cm^{-1} to 1540 cm^{-1} achieved using a coherent spectral width of 6.6 along with a thickness of 201.2 μm.

Similar agreement was also possible for the same transmittance spectra in the wavenumber region from 960 cm^{-1} to 1040 cm^{-1}, as shown in Figure 4.2 (b). Achieving a proper fit necessitated slight adjustments in the optical constant values since using a different thickness in a different wavenumber region for the same measurement would have had no physical basis. As a result, the index of refraction was used as a fitting parameter. Since the thickness of the sample was set to be the same as in the previous

case (201.2 μm), the refractive index of silicon was found to be 3.44, which is within 0.44 percent relative error from the value in Palik's handbook (Edwards, 1985). The coherent spectral width $\delta\bar{\nu}$ for fringe smoothing was 6.2 cm^{-1}, which is less than the value in the wavenumber region of 1460 cm^{-1} to 1540 cm^{-1}. Consequently, the wavenumber-dependent coherent spectral width values for the spectral averaging confirm the decrease in the degree of coherence at shorter wavelengths. For this sample, the instrumental effects such as beam divergence and finite aperture size also reduced the fringe contrast. It should be emphasized that these two wavenumber regions were chosen arbitrarily, and one could have instead used the thickness from the 960 cm^{-1} to 1040 cm^{-1} region and varied *n* in the 1460 cm^{-1} to 1540 cm^{-1} region.

Figure 4.3 shows the spectral reflectance of sample D3. Here, the incidence angle is treated as an adjustable parameter because the actual angle of incidence may deviate slightly from the nominal value in the specifications. An angle of incidence of 10.3 deg and a thickness equal to 245.9 μm were used to fit the free spectral range and the fringe locations, as shown. This value is within 1.6 percent of the nominal thickness. As in the case of the spectral transmittance, the fringe smoothing is necessary to reduce the fringe contrast. The coherent spectral width $\delta\bar{\nu}$ is estimated as 5.4 cm^{-1}, which is very close to the free spectral range, 5.94 cm^{-1}. Since the resolution of the FT-IR spectrometer was set to 1 cm^{-1}, it appears that the beam divergence in the spectrometer may be influencing the degree of coherence in the reflectance measurements, as was found for the transmittance measurements.

4.3 Single-Side Polished Samples

Because the previous samples were double-side polished, it was not possible to examine the effects of rough surfaces. Samples with a rough back side that were also sufficiently thin to allow for clearly defined fringes were sought. Four silicon wafers and a diamond thin film fit these initial criteria. These samples permit the examination of two important aspects of this study: the effects of rough surfaces and the factors that influence partial coherence.

4.3.1 Silicon Wafers

The spectral transmittance of sample S1 was measured and is shown in Figure 4.4. Because the rough side has such a low rms roughness, the wafer could be considered double-side polished, which is apparent with its surface finish. Rough surfaces generally lead to a decrease in the radiative properties at higher wavenumbers due to the wavelength dependence of the scattering factors in Eqs (2.7) and (2.8). The measured transmittance validates the observation that the rough surface is nearly smooth since the exponential decay is not noticeable and the resulting fit assumes that both surfaces have zero rms roughness values. On the other hand, the rms roughness for the rough side obtained from the AFM measurement was 23.3 nm, based on a surface area of 40 nm by 40 nm. The AFM image of the sample, shown in Figure 4.5, indicates that the grinding operation used in the manufacturing process produced a surface that was nonuniform in roughness, resulting in grooved features in a preferred direction. A thickness of 98.8 μm was used to match the fringes in the spectra and a coherent spectral width that was linearly-dependent on the wavenumber was needed for this fit; the constants *a* and *b* were

found to be $1.5 \cdot 10^{-3}$ and 8.9 cm^{-1}, respectively. The predicted and measured fringes correspond fairly well in wavenumber over the mid-IR range, but the maxima and minima of the measured fringes do not match the predicted profile, especially in the 500 to 1200 cm^{-1} wavenumber range, suggesting that a linearly-dependent coherent spectral width may not be suitable in this case. Furthermore, the mean value of the measured transmittance appears to be about 5 percent greater than the corresponding predicted values, particularly at low wavenumbers, when the reduction due to the scattering factors could more easily be neglected.

Figure 4.6 shows the transmittance of a sample S3, which yielded unexpected results. Fitting only the smaller wavenumber range (500 to 700 cm^{-1}) was possible, and the predicted transmittance deviated considerably at shorter wavelengths. The behavior at higher wavenumbers is unusual since with the rough surface, the scattering factor should dominate, given an rms roughness on the order of 1 μm obtained from fitting. The roughness of the non-smooth surface was determined to be 0.81 μm from the profilometer measurement. Interestingly, the transmittance actually starts to increase at around 1500 cm^{-1}. This suggests deficiencies in applying scalar scattering theory to this case and raises questions about exactly what properties of the sample could give rise to this behavior. Insight into this question was made possible by carefully analyzing the surface characteristics.

Figure 4.7 shows the height profile of sample S3. This is representative of the other height profiles measured in this study, which are not shown. The resolution was set to 1 angstrom with a scan length of 1 mm. Leveling the height data was needed to address the possibility that the sample may not have been level when placed in the holder. This

involves performing a linear least-squares fit of the data and then subtracting the value of this line from the height value at a given x position. Overall roughness levels were assumed to be uniform over the sample.

Significant deviation of the measured spectra from predictive curves also occurred when modeling sample S2. Figure 4.8 shows the measured transmittance with several different surface roughnesses for the rough side. The other side was assumed to be perfectly smooth. The predicted curves have been spectral averaged to enhance clarity and show the trends of the fringe-averaged transmittance. The sharp decline in the transmittance near 615 and 1100 cm^{-1} is likely due to optical phonon absorption. Phonons are quanta of lattice vibrations in crystalline solids, and absorption by lattice vibrations is due to the existence of electric dipoles formed by the atoms in semiconductors (Zhang et al., 2003). For typical rms roughness values, the expectation is that the decay term dominates at shorter wavelengths. However, the measurement shows that there is very little decrease over the wavenumber span. When low roughness values were used, the mean value of the predicted transmittance was higher than the measured values by over 15 percent. A backside roughness of 0.7 μm, as determined from the profilometer measurement, was insufficient to obtain a proper fit. The profilometer used the same settings and leveling corrections as sample S3.

The disagreement seen in the spectra of sample S2 is symptomatic of the problem arising in the case of sample S3. Figure 4.9 shows an image of sample S3 taken with an optical microscope set at 200X magnification, and Figure 4.10 shows a similar image of sample S2 taken at 50X magnification. By revealing unusual grain-like microstructures, both of these images may offer clues to the large error between predicted and measured

transmittance. These grain-like features are unexpected, and absent in Figure 4.11, which shows an image of the rough side of sample S4. The round features in the image of sample S2 probably result from etching, which is one way to reduce the thickness during the manufacturing process. Caustic etching, which was most likely used here, typically does not produce a uniformly flat surface. The image of sample S3 shows square-shaped features because the surface was lapped, a process similar to grinding. In this case the lapping was so aggressive that shear occurred, revealing square-shaped features produced by the crystal structure of silicon. Although the square-shaped features of sample S3 are far smaller than the round shapes of sample S2, both types of features are larger than the surface imperfections found on the rough surfaces of many other thin-film samples.

Scalar scattering theory is based on a wave-optics approximation, and most likely there is a suitable spectral range and range of surface roughnesses for which scalar scattering theory is valid. That range may be one in which the surfaces are optically smooth–that is, the surface imperfections are much smaller than the radiation wavelength (Siegel and Howell, 2002). The spectrum of sample S3 shows that there is agreement at long wavelengths, and the predictions deviate from the measurements at shorter wavelengths. The effect of the large microstructures, which may be more accurately modeled by geometric optics, may be dominant compared to the effect of the smaller surface roughness, which can be addressed by scalar scattering theory. The ultimate result is scalar scattering theory may not be effective in this regime.

Figure 4.12 shows the transmittance of sample S4 which yielded the best agreement between predictions and measurements among the single-side polished silicon samples. A rapid decrease in the signal near the cutoff wavenumber caused the spectrum

to become noisier toward 500 cm^{-1} although this may be difficult to see in the plot shown. Phonon absorption is again noticeable near 615 and 1100 cm^{-1} wavenumbers. The overall agreement of the transmittance is clearly an improvement over the case for the 150 μm sample with scattering leading to an exponential decay at higher wavenumbers. In this case, the coherent spectral width is constant and equal to 0.29 cm^{-1}. An enlarged view shows that the agreement in the fringe positions can be good at certain wavenumbers, though at shorter wavelengths the agreement gradually worsens, and separate fittings may be needed as was done for sample D2. The thickness of the sample, leading to a small free spectral range, makes clearly delineating the fringes a difficult task. The rms surface roughness of the rough side obtained using the profilometer was 0.40 μm, which is on the order of that obtained through fitting, 0.56 μm.

Figures 4.13 and 4.14 show the reflectance of sample S4. The predictions captured the general trends well, particularly for the case of radiation incident on the smooth side. The angle of incidence was assumed to be 10 deg for both cases. One side was assumed to be perfectly smooth, and the rms surface roughness of the rough side obtained from fitting was 0.55 μm, which is within 2 percent of the value determined from the transmittance prediction. The fitted thickness was found to be 505.5 μm, which is slightly less than the value from the transmittance fitting, 508.5 μm. The thickness measured using the micrometer was determined to be 502.9 ± 5.1 μm. Water vapor absorption is apparent near 1500 and 3900 cm^{-1}. Enlarged plots reveal reasonable agreement in the fringe positions. Matching the fringe contrast for the case of radiation incident on the rough side proved to be difficult when using linearly dependent coherent spectral widths.

4.3.2 The CVD Diamond Thin Film

Many of the challenges encountered when modeling the single side rough silicon wafers did not arise in the case of the CVD diamond film, sample C1. Photographs taken at the highest magnification of the microscope show a relatively uniform rough side. Figure 4.15 shows the normal transmittance of the diamond film, and it is clear that fringe smoothing led to excellent agreement with the measured spectrum. The slight offset noticeable near 2900 cm^{-1} may result from water vapor absorption. In this case, setting the spectrometer's resolution to 4 cm^{-1} was sufficient to clearly observe the fringes since the free spectral range was over 200 cm^{-1}. From the transmittance curve fitting, the thickness of the diamond film was estimated to be 11.5 μm based on the peak locations. It is important to note that some measurements of the diamond film taken under similar conditions yielded spectra with fringes that appeared shifted from each other, in some cases by as much as half the free spectral range. This was probably due to variations in the film's thickness and the beam spot location, which changed as the sample was translated. The optical constant data taken from Palik's handbook (Edwards and Phillip, 1985) was for crystal diamond (type IIa). By fitting the transmittance in the short wavelength region, the rms roughnesses of the top and bottom surfaces were estimated to be 0.31 μm and 0.15 μm, respectively. A non-zero roughness for the bottom surface was needed to obtain a reasonable fit. Without fringe smoothing, the predicted fringe contrast is large, particularly in the longer wavelength region. The fringe contrast decreases significantly as the wavenumber increases, reaching zero somewhere between 1500 cm^{-1} and 2000 cm^{-1}. As explained in Chapter 2, when the coherent spectral width

equals the free spectral range, the fringes disappear after fringe averaging, and when $\delta\overline{\nu} > \Delta\overline{\nu}$, the peaks and valleys of the fringes interchange after fringe smoothing, which indeed appears to happen above 2000 cm^{-1}, as shown in Figure 4.15 (b). The constants *a* and *b* used in the fringe smoothing were found to be 0.1 and 20 cm^{-1}, respectively.

It can be shown that the normal transmittance is independent of which surface is on the top or bottom, and measurements appear to confirm this fact. In modeling the transmittance of the diamond sample, adjusting the refractive indices were needed to reduce an offset between the measured and predicted spectra that would otherwise have formed around 1000 to 1500 cm^{-1}. The plot shown in Figure 4.15 reflects the lower refractive index values that were needed (about 2.2 rather than 2.38). The physical explanation is that the original tabulated values were suitable for monocrystalline diamond while sample C1 used in the measurements consists of polycrystalline layers with small voids and gaps between the layers. This leads to lower refractive indices than those of monocrystalline diamond. Petrich and Stenzel (1994) noted similar deviations in their determination of the optical constants of CVD diamond film, attributing the effect to the polycrystalline structure of the material.

Figure 4.16 (a) shows the reflectance of the diamond film when the radiation is incident on the rougher side. As was the case for the transmittance, the interference oscillations of the reflectance gradually diminish in strength, eventually dying out around 4000 cm^{-1}. By matching the free spectral range and fringe locations, the thickness of the diamond film was determined to be 12.2 μm, which is within 22 percent of the nominal thickness. Unlike in the case of the transmittance, though, it was impossible to fit both the free spectral range and the fringe locations simultaneously using the best fits when taking

thickness as the only adjustable parameter. The rms roughnesses of the rough and smooth surfaces were assumed to be 0.31 μm and 0 μm, respectively, which differ from the transmittance fitting. Although the diamond may have a large total thickness variation, the surface roughness values should be about the same for different measurements. This issue has yet to be explained, and may be resolved through better fitting methods. In order to fit the fringes, spectral averaging was conducted with the following wavenumber-dependent coherent spectral width: $\delta\bar{\nu} = 0.04\bar{\nu} + 76 \ \text{cm}^{-1}$.

When the radiation is incident on the smoother side, as plotted in Figure 4.16 (b), not only does the fringe contrast decrease with higher wavenumber, but the reflectance settles to an almost constant value. The same roughness parameters (rms roughness) were used as in the other reflectance prediction. The diamond film thickness was found to be 12 μm after fitting the free spectral range. This value is within 0.2 percent of the value obtained from the previous reflectance measurement and within 5 percent of the thickness determined from the transmittance measurement. For the fringe smoothing, the coherent spectral width was $\delta\bar{\nu} = 0.07\bar{\nu} + 58.0 \ \text{cm}^{-1}$, which differs from that of the previous case. These differences indicate that sample and surface characteristics as well as instrumental effects contribute to the partial coherence of the radiation.

A variety of effects may be causing the lack of agreement between the measured and predicted reflectance in both the smooth side- and rough side-incident cases. One possibility is that the angle of incidence of the beam may not correspond to the nominal value. Changing the angle of incidence in the model did not appear to significantly affect the fringe locations, however, and the reflectance does not seem to be very sensitive to slight adjustments in an incidence angle that is near normal. Systematic errors in the

reflectance accessory that become significant when measuring rough samples may also be a contributing factor. Another possible cause may be the conical nature of the reflectance measurement, illustrated in Figure 3.3. Properly modeling the reflectance requires integrating over a finite solid angle, and the resulting value is not necessarily the value at the average incidence angle. The equation for the reflectance is as follows:

$$R = 2\pi \cos(\theta) \int_0^{\theta_{hc}} f_r \cos\theta' \sin\theta' d\theta' \qquad (4.3)$$

where θ_{hc} is the half cone angle for the receiving solid angle and f_r is the so-called bidirectional reflectance distribution function (BRDF), commonly used to describe the reflection of radiation from real surfaces (Shen et al., 2003). In any case, additional analysis is required to more fully explain the discrepancies in the diamond film reflectance. AFM measurements, shown in Figure 4.17, yielded an rms surface roughness value for the rough side that closely matches the value determined from fitting both the reflectance and the transmittance.

Table 4.1: Summary of sample descriptions.

Sample Name	Material	Polish (SSP/DSP)	Thickness (μm)	Resistivity (ohm-cm)	Measurements	Figure
D1	Silicon	DSP	35	0.001-0.005	Transmittance	4.1
S1	Silicon	SSP	100	> 100	Transmittance	4.4
S2	Silicon	SSP	150	6-7	Transmittance	4.8
D2	Silicon	DSP	200	2000-4000	Transmittance	4.2
D3	Silicon	DSP	250	N/A	Reflectance	4.3
S3	Silicon	SSP	300	> 100	Transmittance	4.6
S4	Silicon	SSP	500	N/A	Transmittance, Reflectance	4.12, 4.13
C1	Diamond	SSP	10	N/A	Transmittance, Reflectance	4.15, 4.16

Table 4.2: Comparison of surface roughness statistics.

	Fitted	Topographic data	
Sample Name	RMS roughness (μm)	RMS roughness (μm)	Autocorrelation length (μm)
S1	0	0.023[a]	N/A
S2	N/A	0.68 ± 0.15	35.8 ± 1.2
S3	0.9	0.815 ± 0.027	12.3 ± 1.5
S4	0.56 (T) 0.55 (R)	0.404 ± 0.024	5.69 ± 0.36
C1	0.31 (T) 0.15 (T) 0.31 (R) 0.0 (R)	0.316[a]	N/A

a. Denotes data from AFM. All other data from surface profilometer.

Table 4.3: Summary of coherent spectral widths with instrumental resolutions.

Figure	Sample Name	Measurements	Fitted thickness (μm)	Free spectral range[a] (cm^{-1})	Coherent spectral width[b] (cm^{-1})
4.1	D1	Transmittance	35.4	41.25	$0.0056 \cdot \bar{\nu} + 4.3$
4.2	D2	Transmittance	201.2	7.26	6.6 (at 1500 cm^{-1}) 6.2 (at 1000 cm^{-1})
4.3	D3	Reflectance	245.9	5.94	5.4
4.4	S1	Transmittance	98.8	14.79	$1.5 \cdot 10^{-3} \cdot \bar{\nu} + 8.9$
4.6	S3	Transmittance	300.0	4.87	n/a
4.8	S2	Transmittance	154.0	9.49	n/a
4.12	S4	Transmittance	508.5	2.87	0.57
4.13	S4	Reflectance	505.5	2.88	$1.7 \cdot 10^{-3} \cdot \bar{\nu} + 0.86$ (smooth incident) $3.8 \cdot 10^{-4} \cdot \bar{\nu} + 1.8$ (rough incident)
4.15	C1	Transmittance	11.5	175.3	$0.1 \cdot \bar{\nu} + 20$
4.16	C1	Reflectance	12.2 (rough) 12.0 (smooth)	175.3	$0.04 \cdot \bar{\nu} + 76$ (rough) $0.07 \cdot \bar{\nu} + 58$ (smooth)

a. Free spectral ranges computed at 1000 cm^{-1}.

b. All instrumental resolutions set to 1 cm^{-1} for silicon and 4 cm^{-1} for diamond.

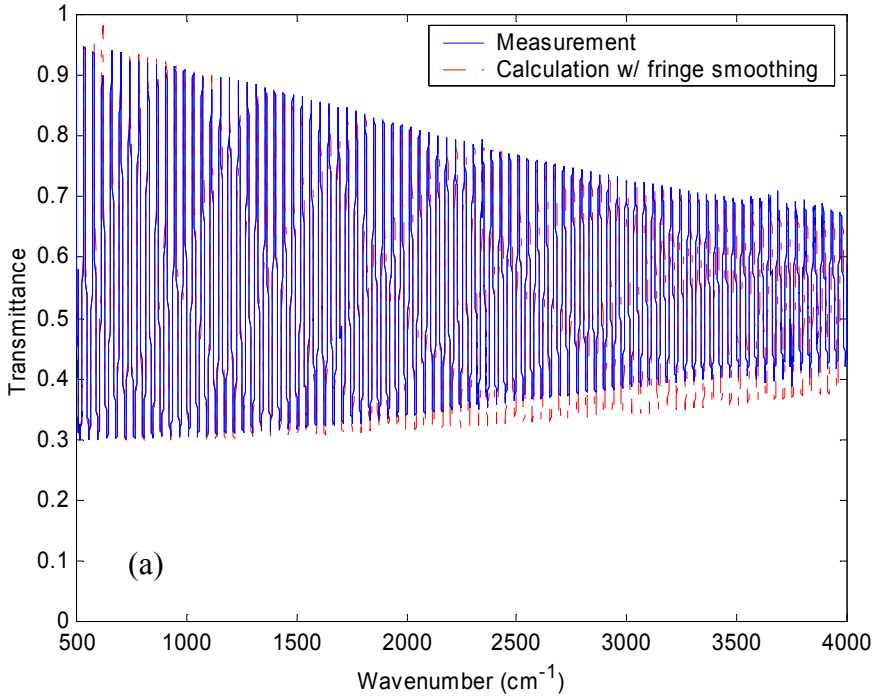

Figure 4.1: Spectral transmittance of sample D1 with smooth surfaces:

(a) from 500 to 4000 cm^{-1}.

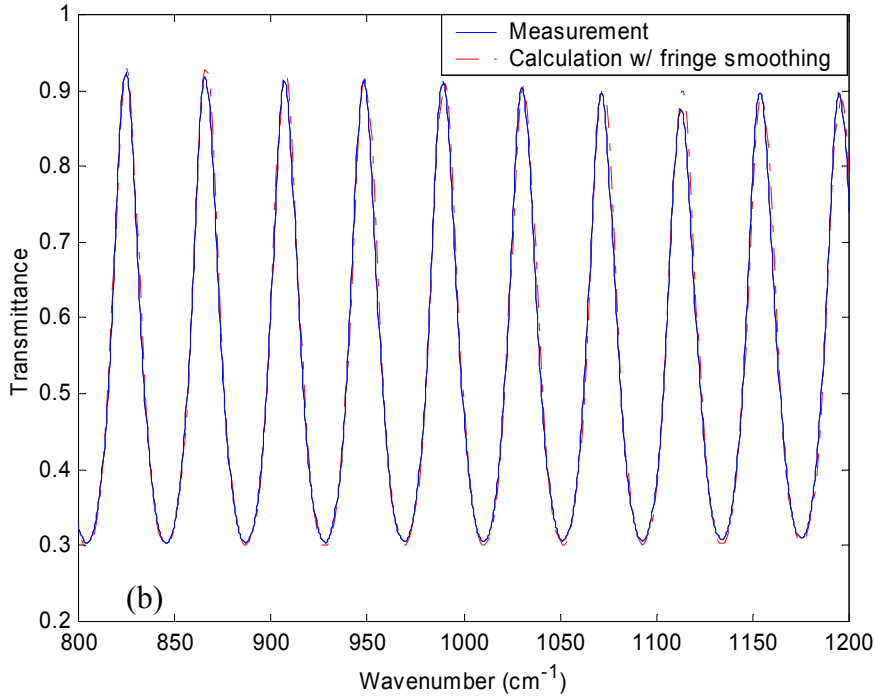

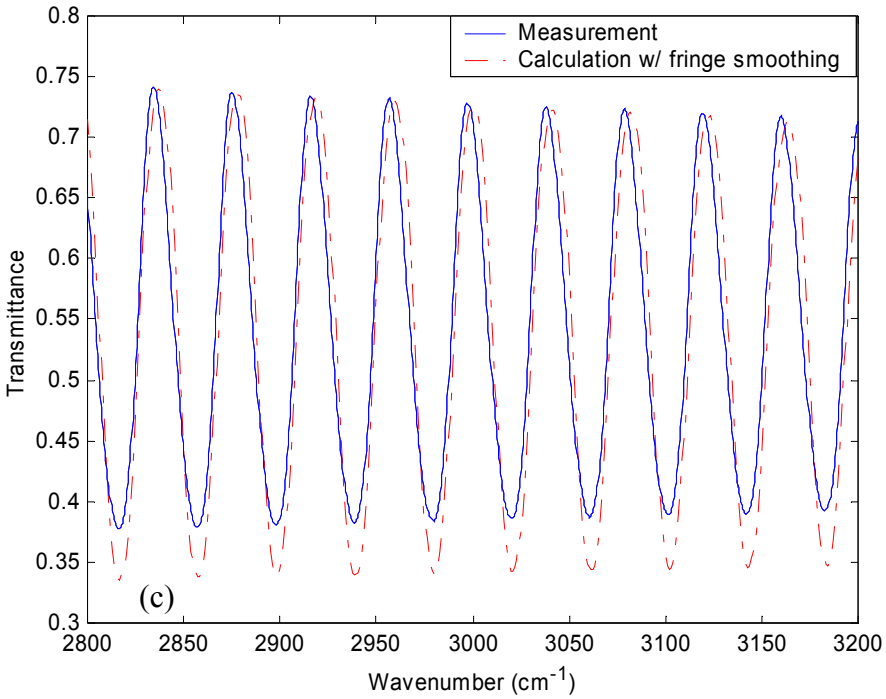

Figure 4.1: Spectral transmittance of sample D1:

(b) from 800 to 1200 cm^{-1}; (c) from 2800 to 3200 cm^{-1}.

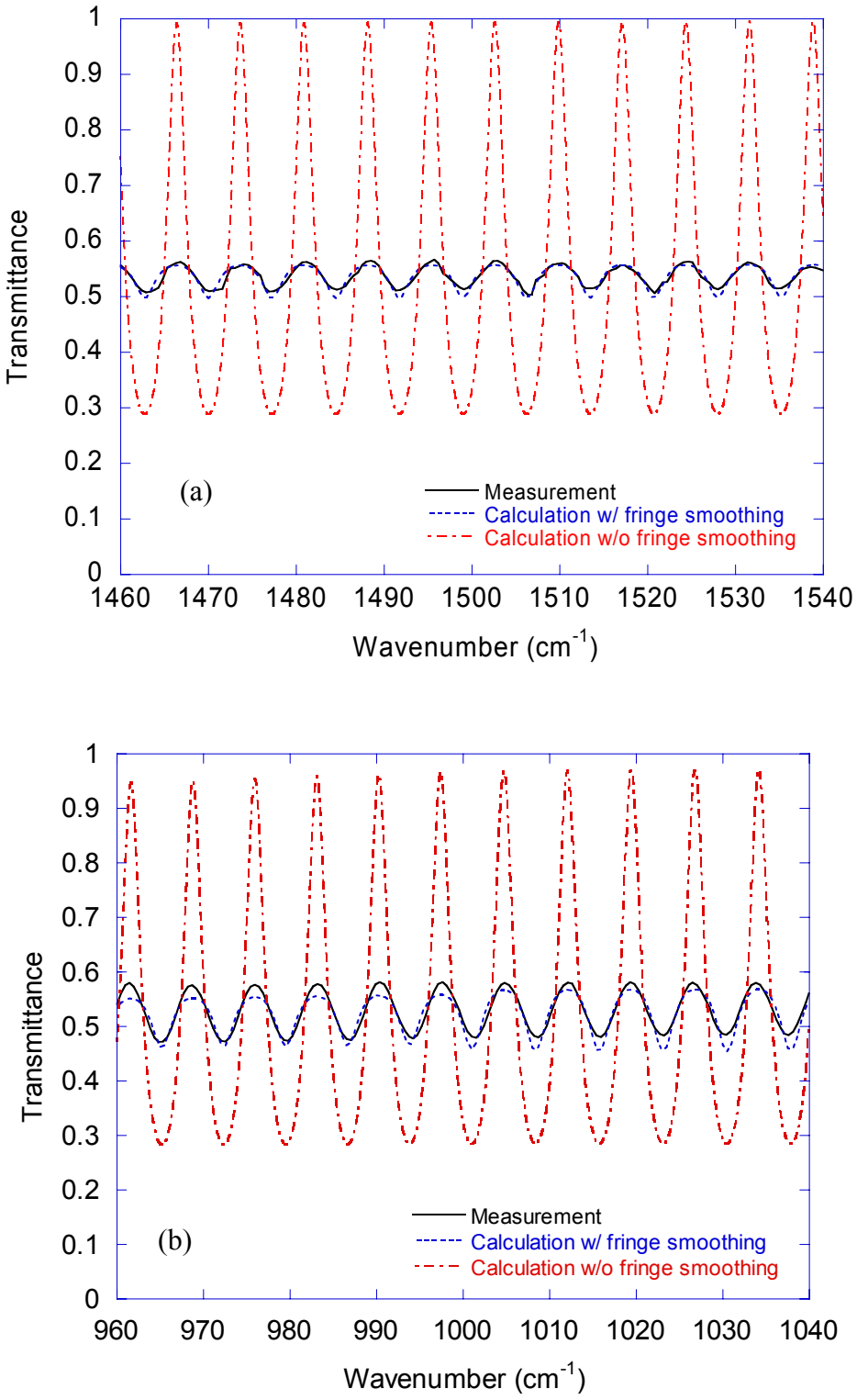

Figure 4.2: Spectral transmittance of sample D2:

(a) centered at 1500 cm^{-1}; (b) centered at 1000 cm^{-1}.

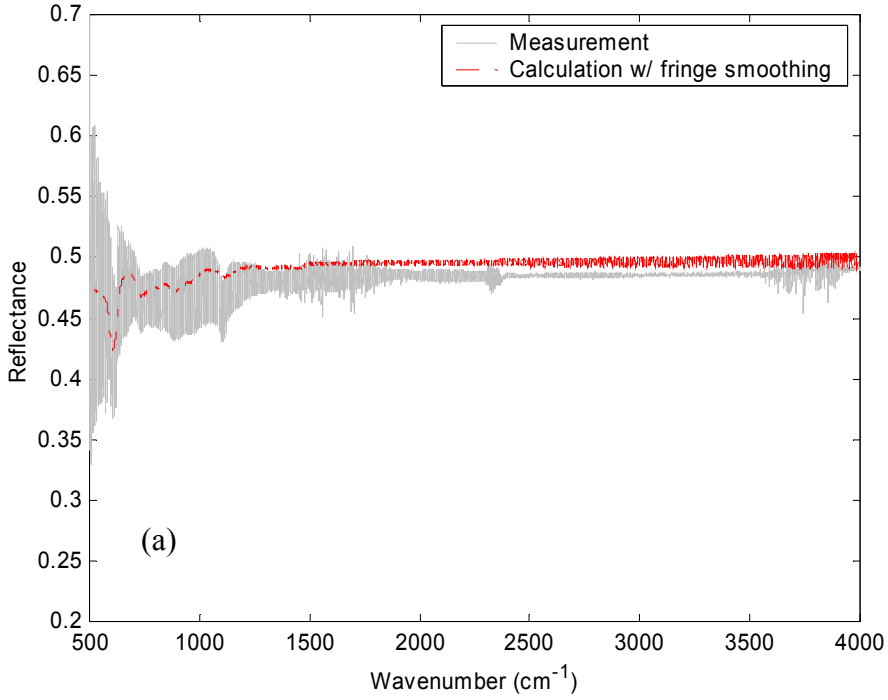

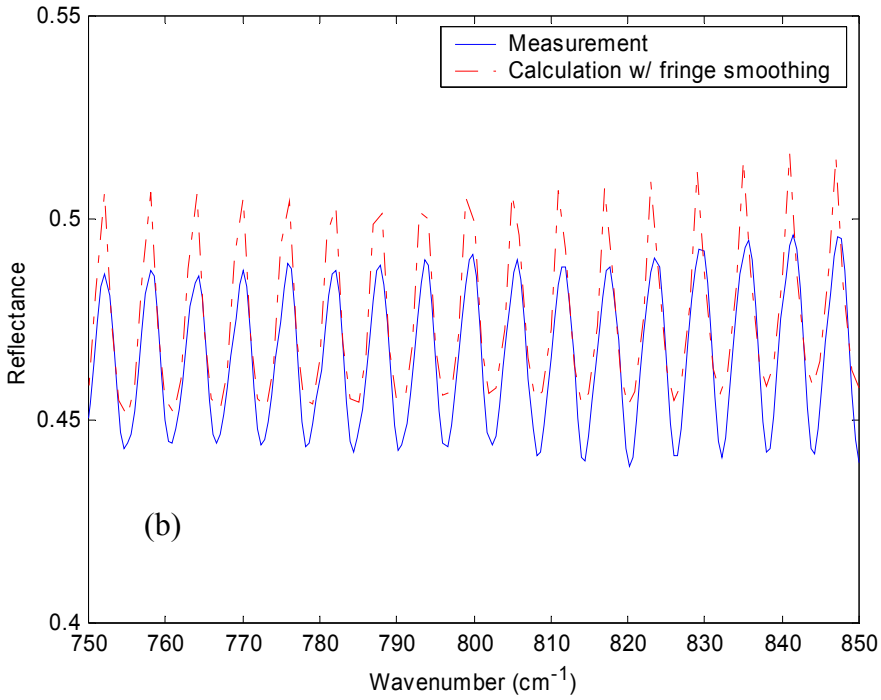

Figure 4.3: Spectral reflectance of sample D3:

(a) from 500 to 4000 cm^{-1}; (b) from 750 to 850 cm^{-1}.

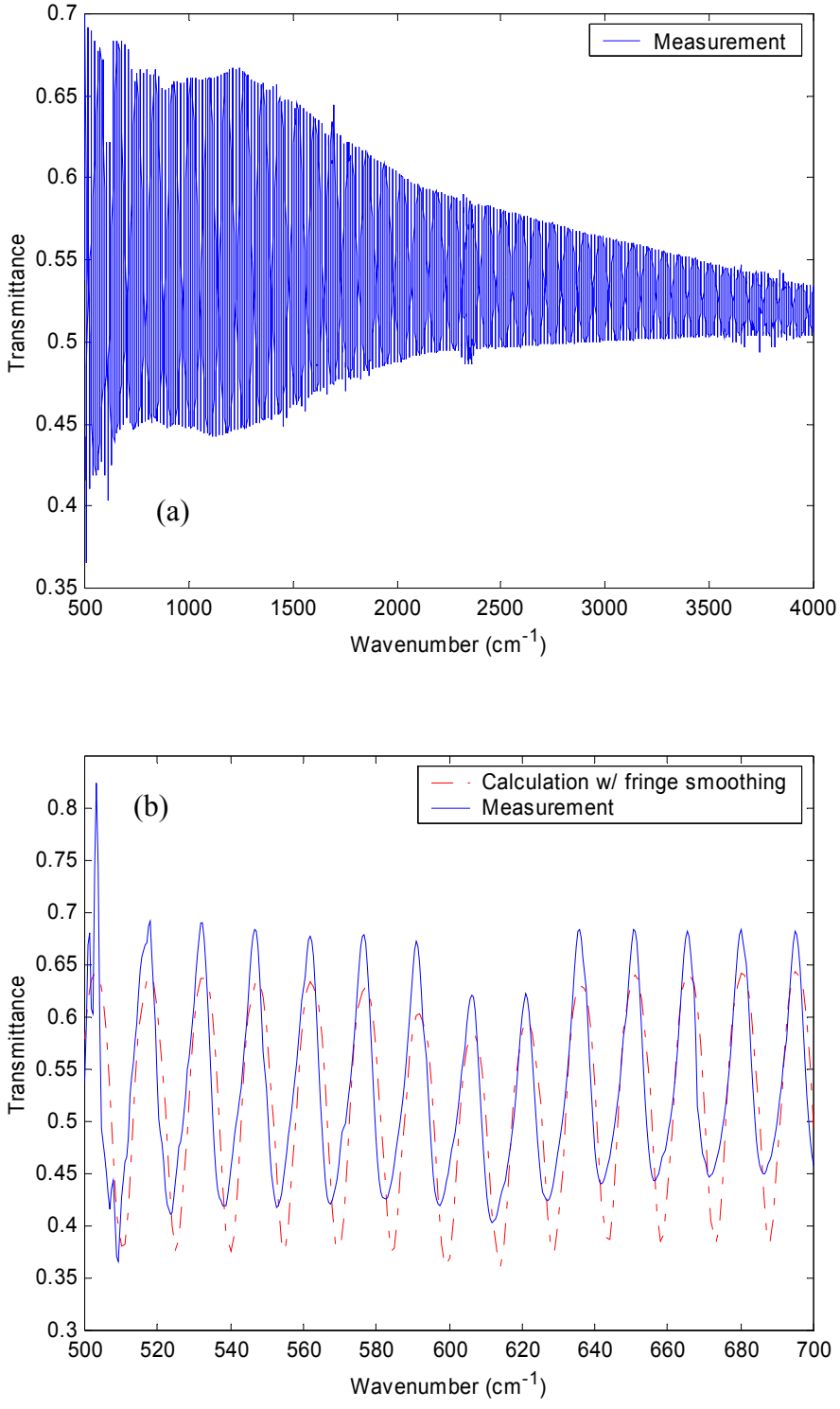

Figure 4.4: Spectral transmittance of sample S1:

(a) from 500 to 4000 cm^{-1}; (b) from 500 to 700 cm^{-1}.

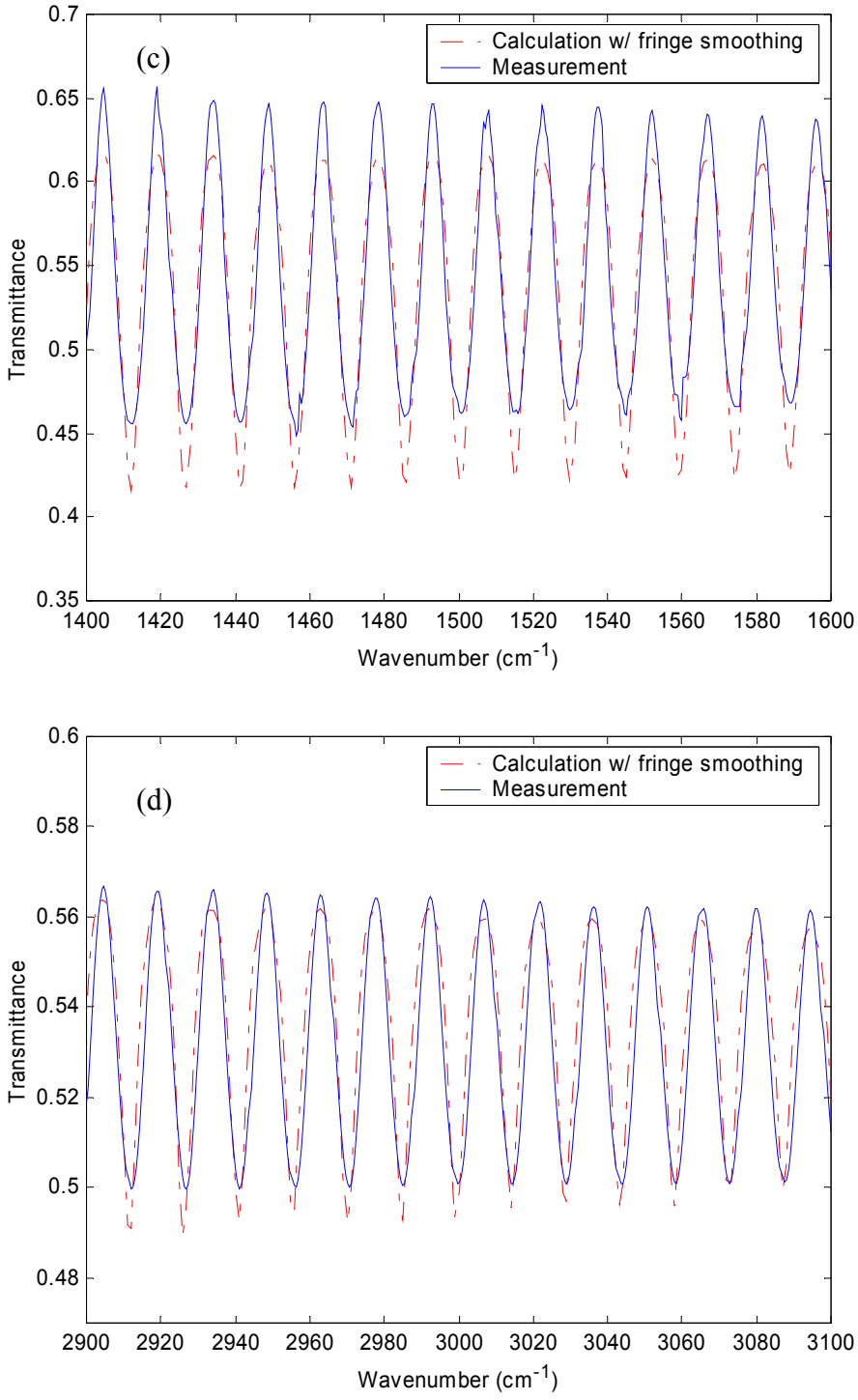

Figure 4.4: Spectral transmittance of sample S1:

(c) from 1400 to 1600 cm^{-1}; (d) from 2900 to 3100 cm^{-1}.

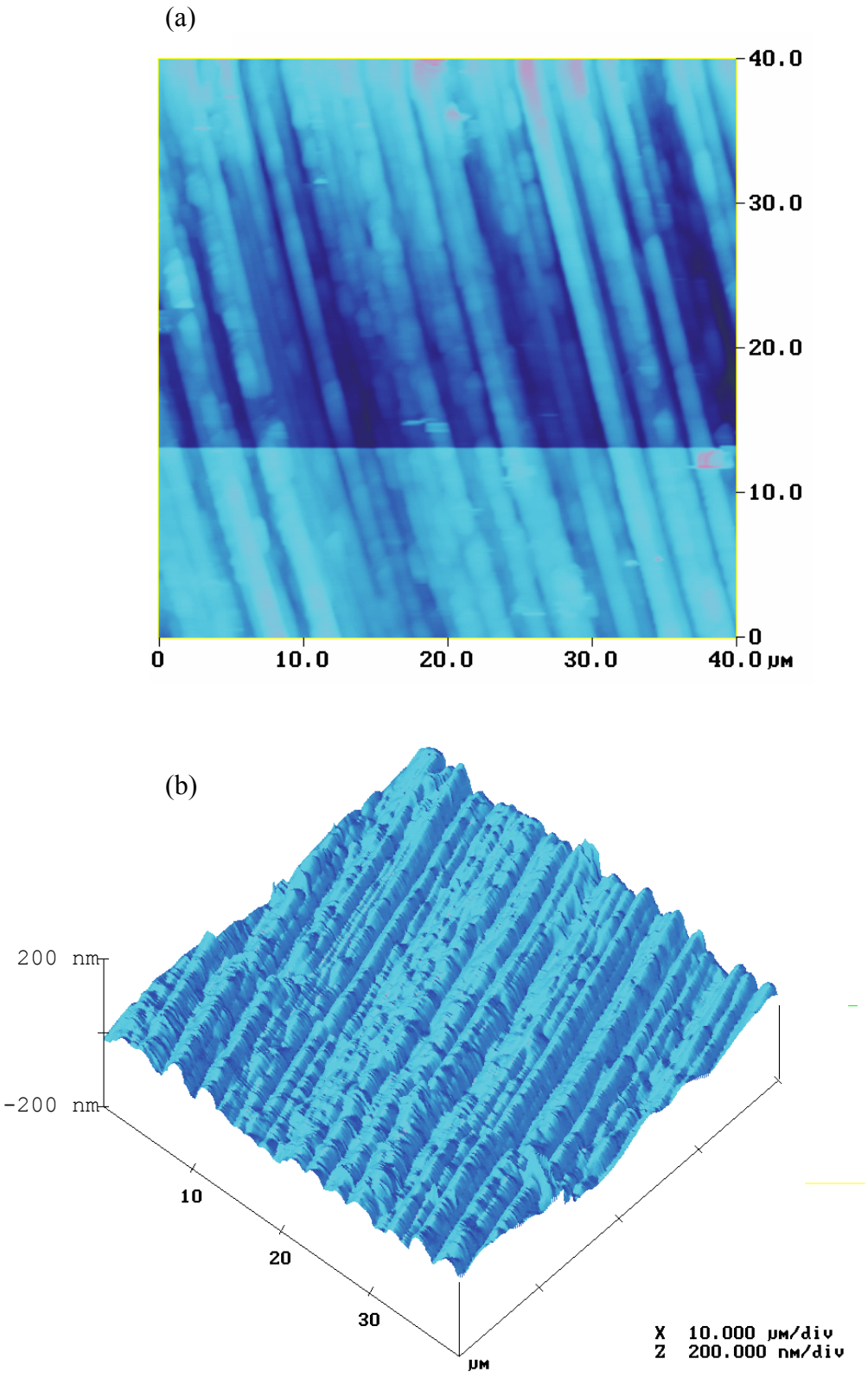

Figure 4.5: AFM image of sample S1: (a) 2-D; (b) 3-D.

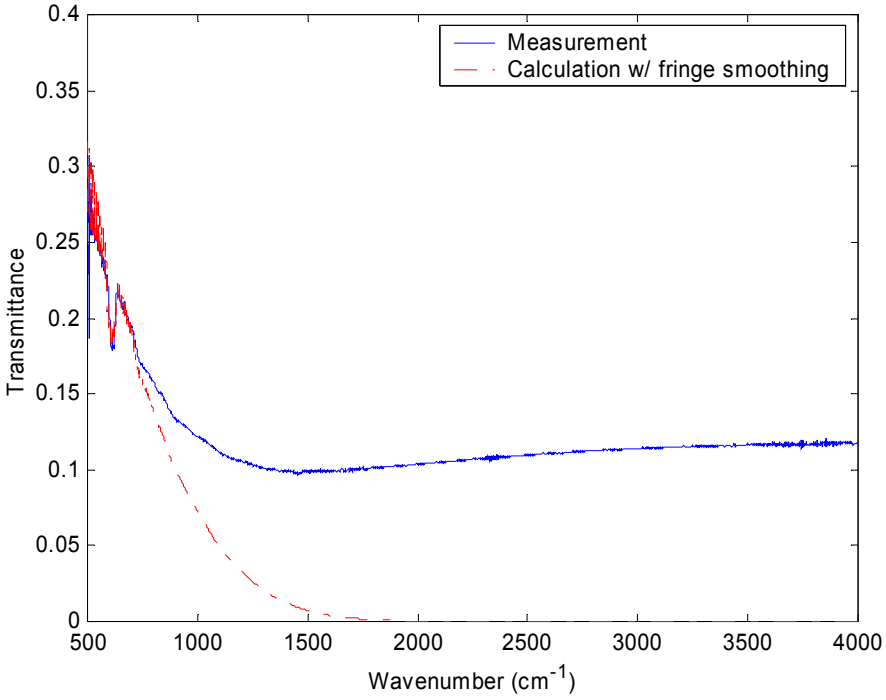

Figure 4.6: Spectral transmittance of sample S3.

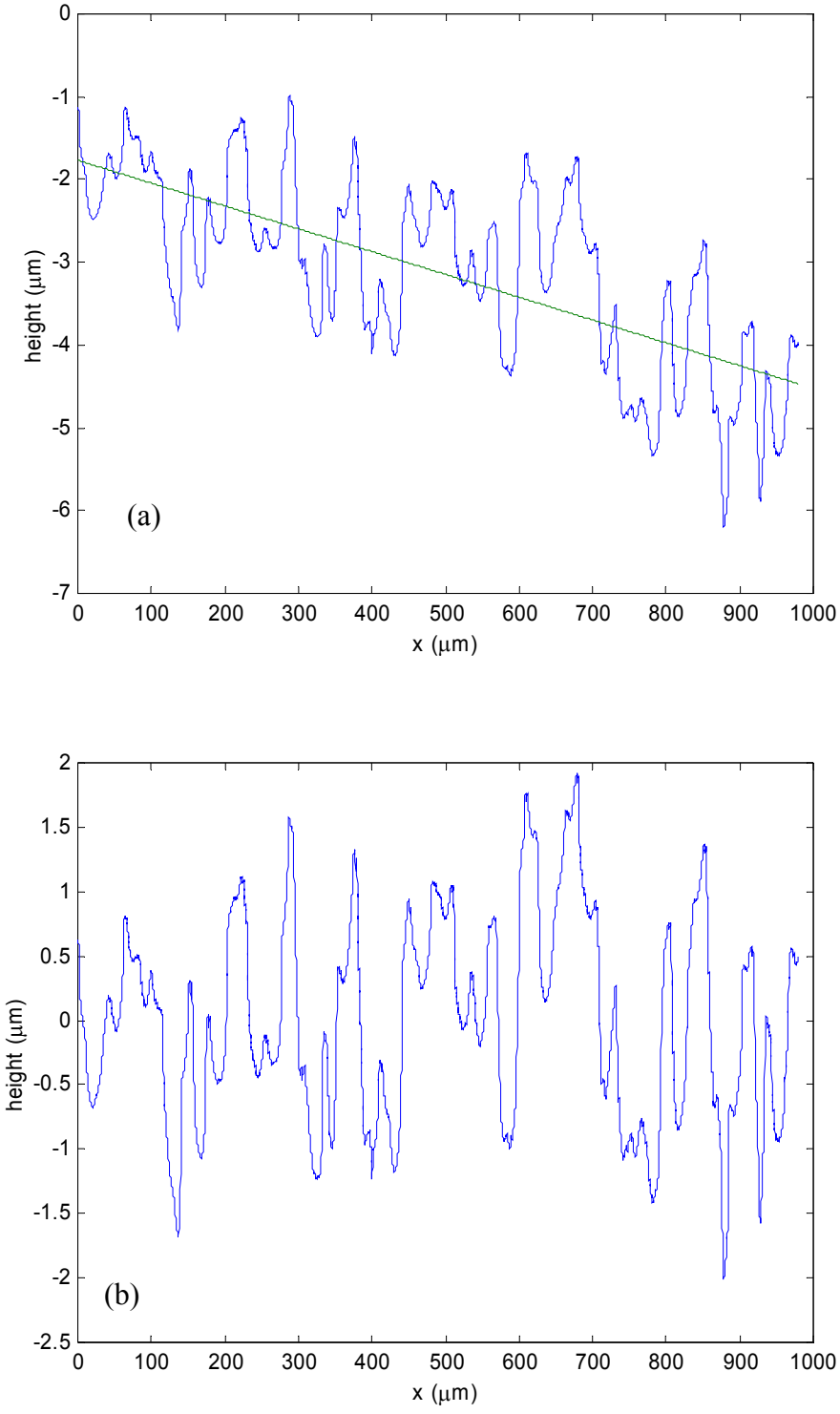

Figure 4.7: Height profile of sample S3 using surface profilometer:

(a) before leveling; (b) after leveling.

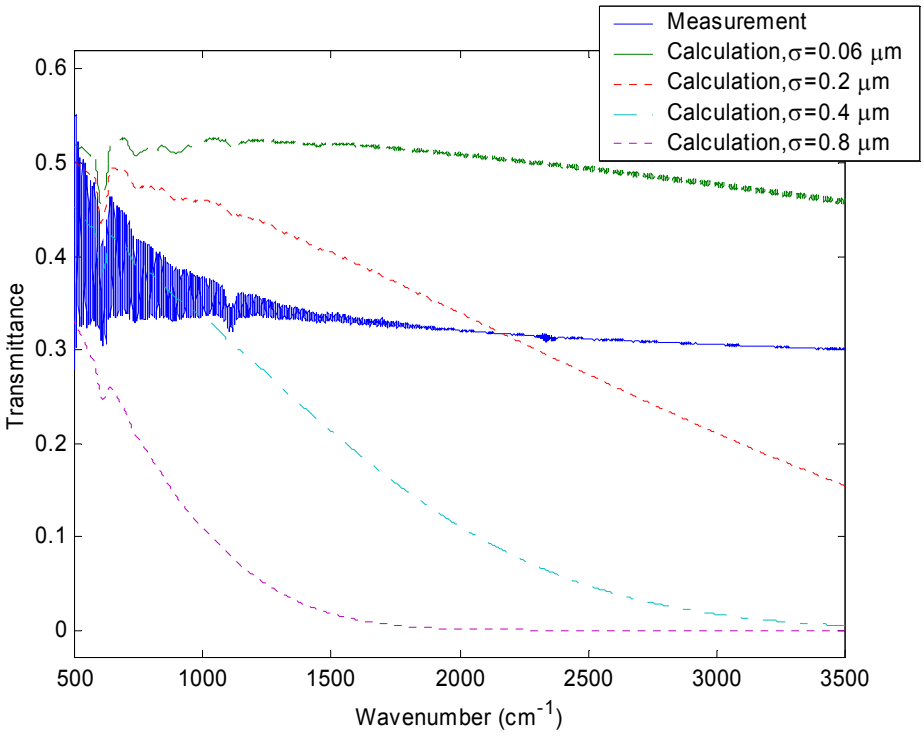

Figure 4.8: Spectral transmittance of sample S2.

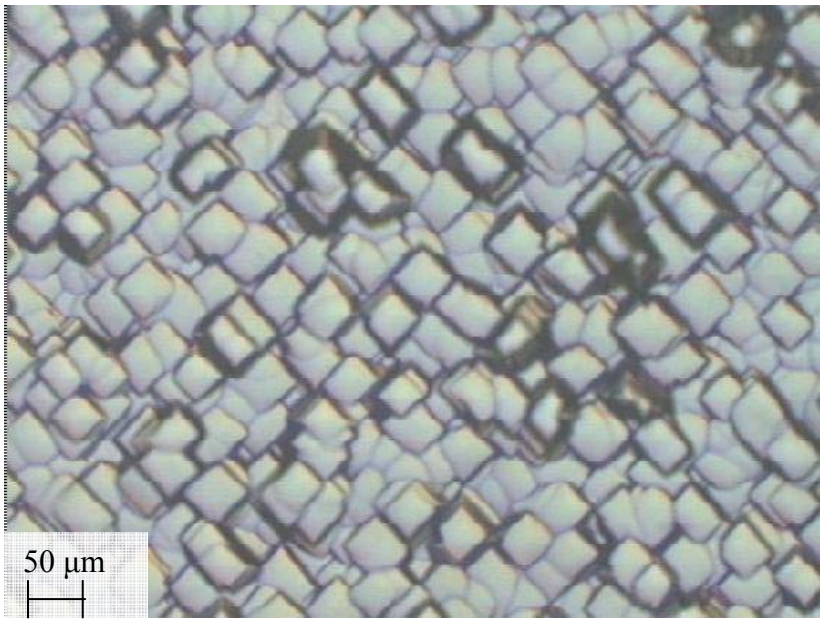

Figure 4.9: Photograph of sample S3 (200X magnification).

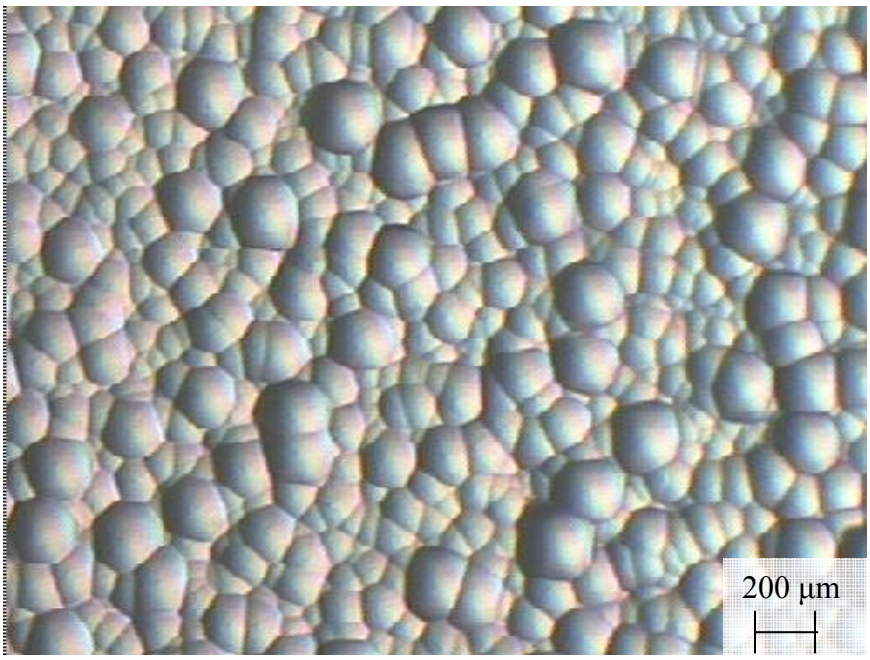

Figure 4.10: Photograph of sample S2 (50X magnification).

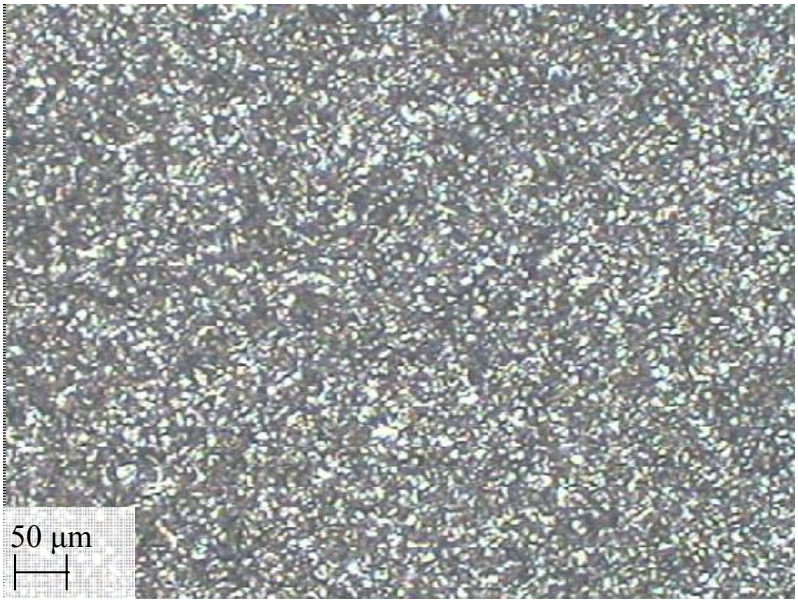

Figure 4.11: Photograph of sample S4 (200X magnification).

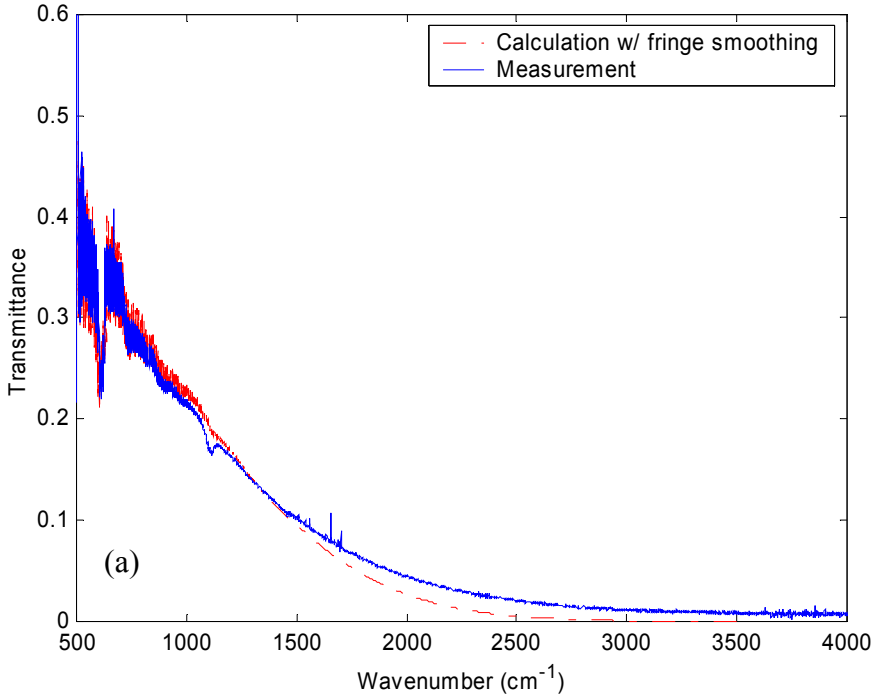

Figure 4.12: Spectral transmittance of sample S4: (a) from 500 to 4000 cm^{-1}.

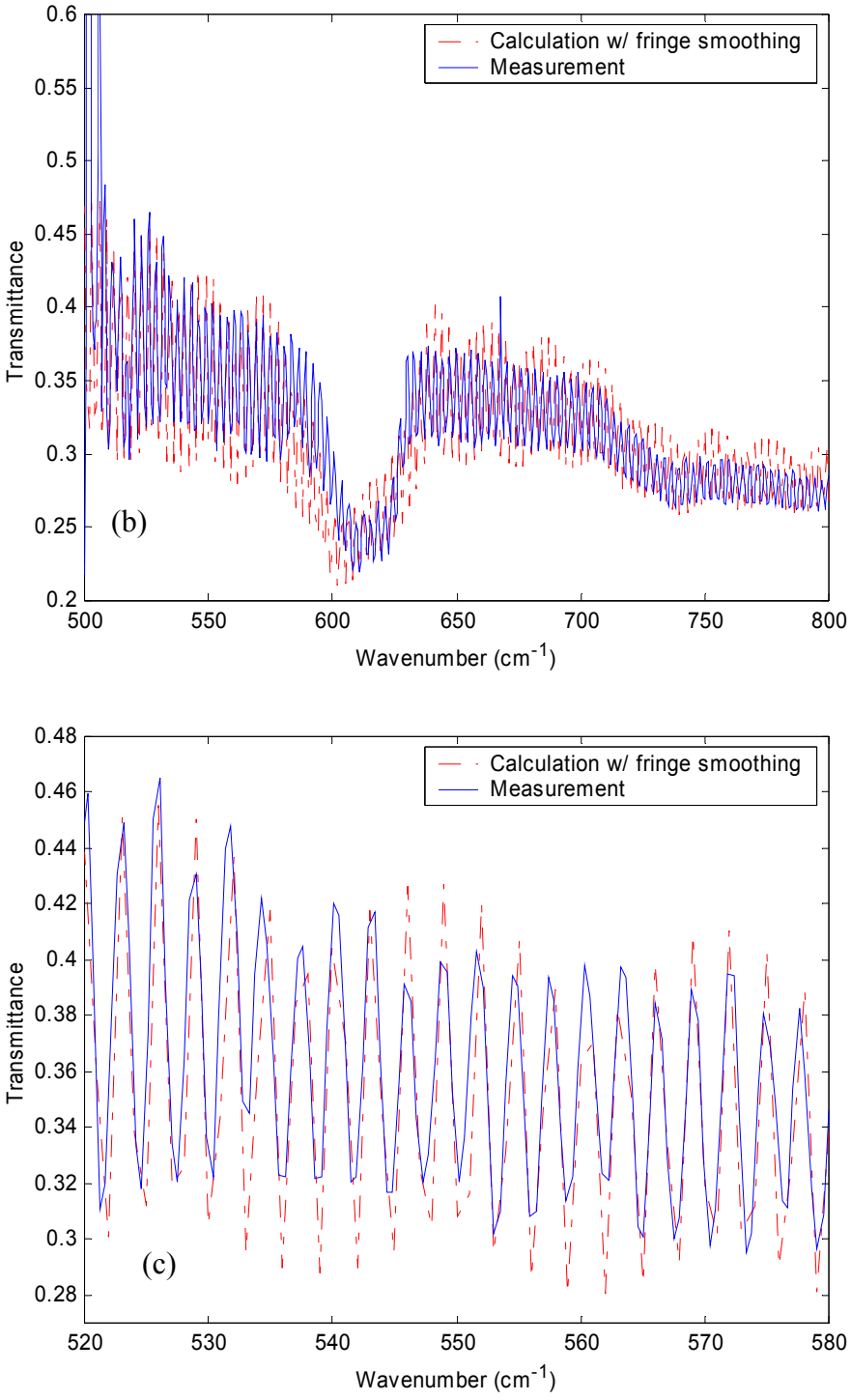

Figure 4.12: Spectral transmittance of sample S4:

(b) from 500 to 800 cm^{-1}; (c) from 520 to 580 cm^{-1}.

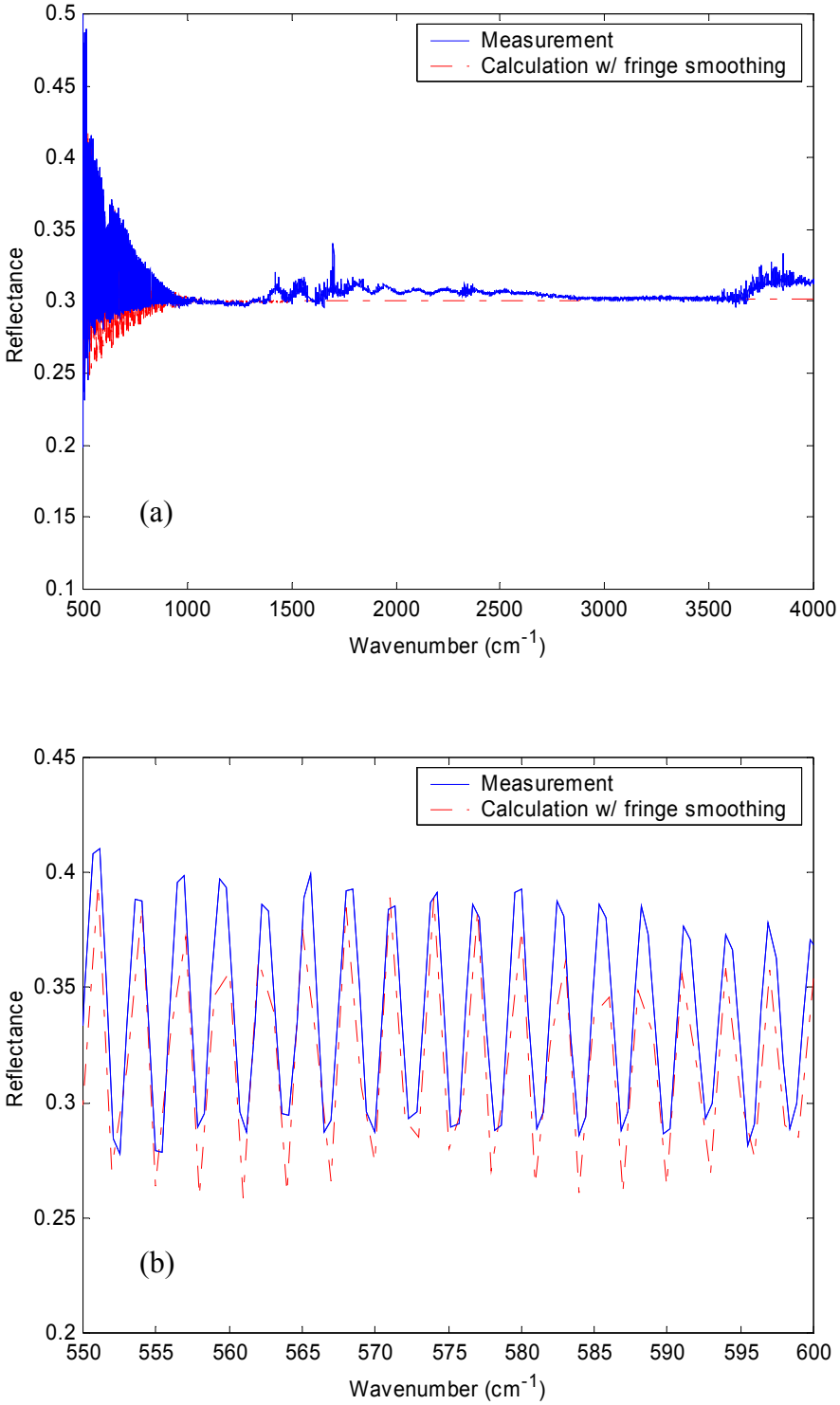

Figure 4.13: Spectral reflectance of sample S4 (radiation incident on smoother side): (a) from 500 to 4000 cm^{-1}; (b) from 550 to 600 cm^{-1}.

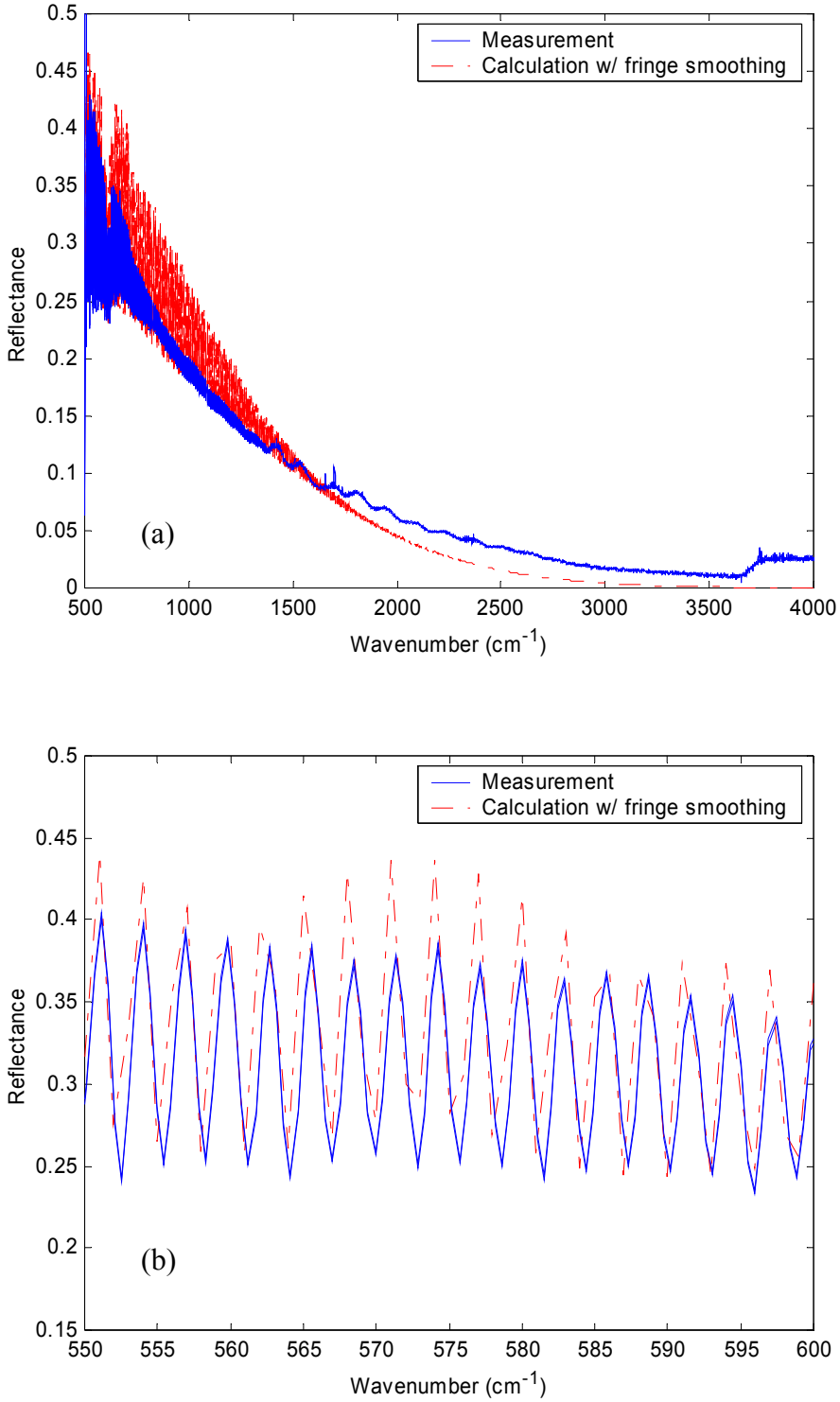

Figure 4.14: Spectral reflectance of sample S4 (radiation incident on rougher side): (a) from 500 to 4000 cm^{-1}; (b) from 550 to 600 cm^{-1}.

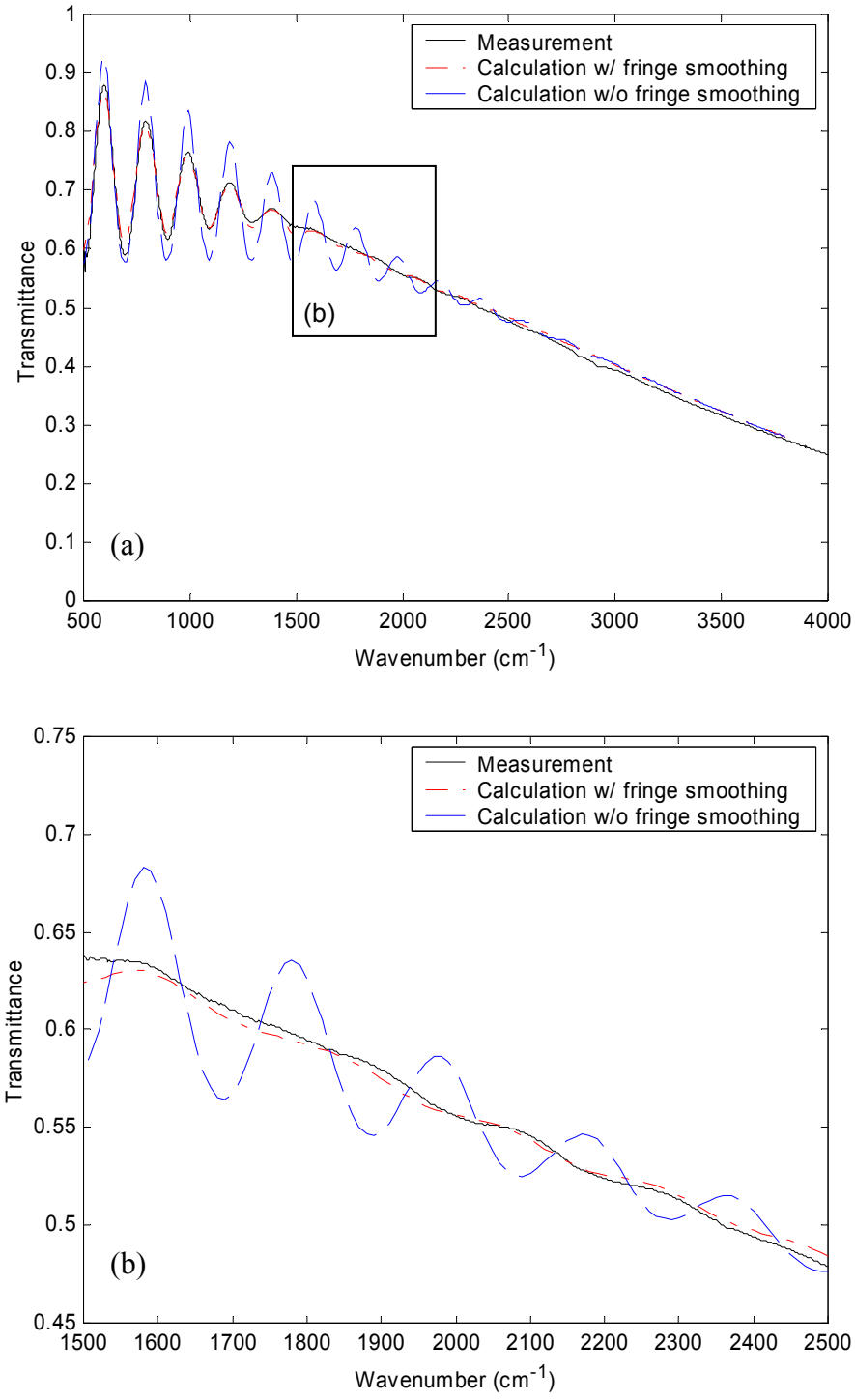

Figure 4.15: Spectral transmittance of sample C1:

(a) from 500 cm^{-1} to 5000 cm^{-1}; (b) from 1500 cm^{-1} to 2500 cm^{-1}.

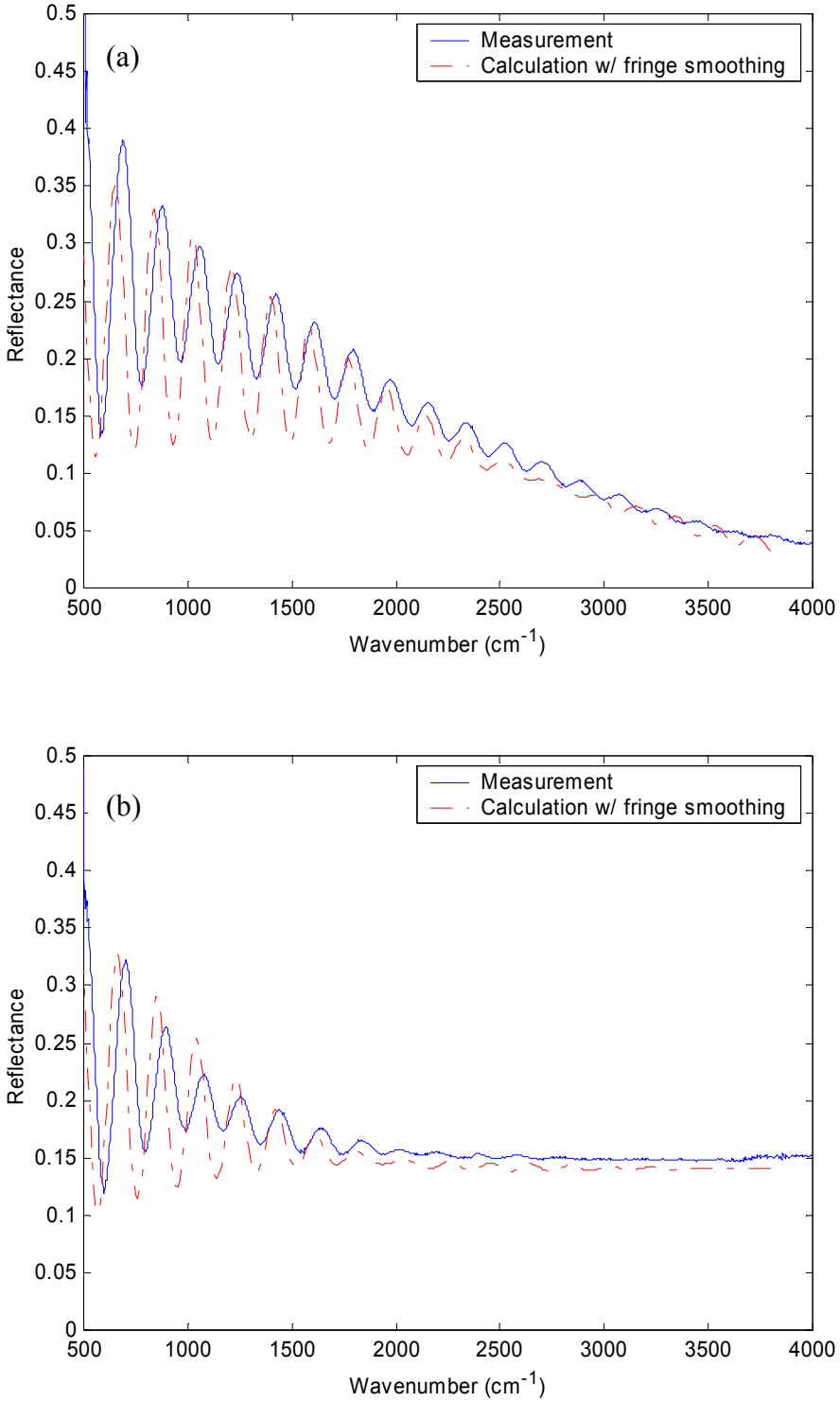

Figure 4.16: Spectral reflectance of sample C1:

(a) radiation incident on rougher side; (b) radiation incident on smoother side.

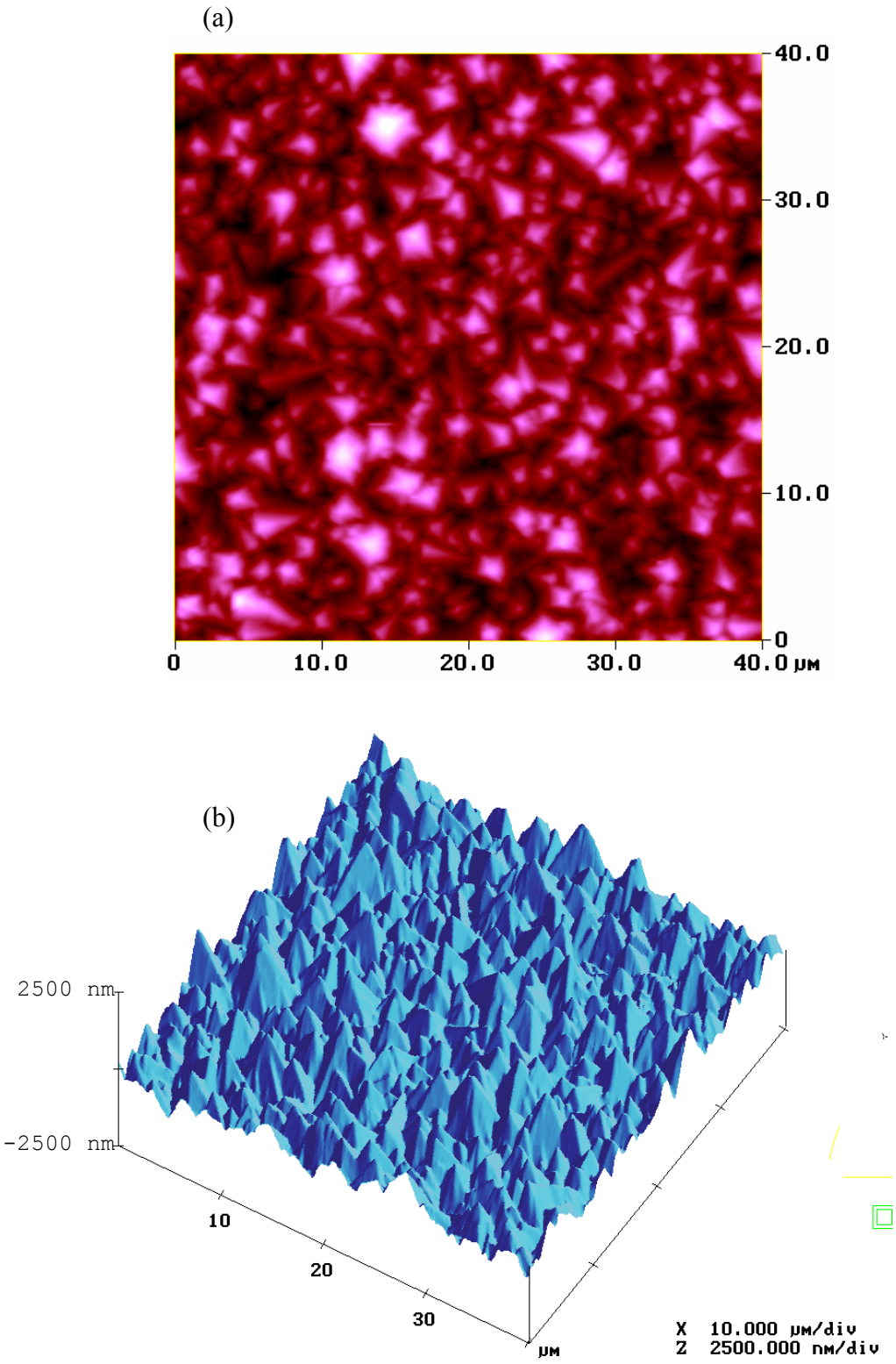

Figure 4.17: AFM image of sample C1: (a) 2-D; (b) 3-D.

CHAPTER 5

CONCLUSION

5.1 Summary

This study is devoted to modeling the radiative properties of thin films with rough surfaces. The focus is on two main issues: partial coherence and rough surface effects. The approach is to predict the transmittance and reflectance of silicon wafers and a CVD diamond film, to obtain measurements of these samples, and to make comparisons between calculated and measured spectra.

5.1.1 Partial Coherence

Partial coherence was addressed in this work by using spectral averaging. Previous research employing partial coherence theory often used the degree of coherence to quantify the coherence of the incident radiation. This study introduced the coherence function to provide an intuitive measure of the coherence of the radiation and is useful for providing information about fringe flipping, which the degree of coherence does not do.

To analyze the effects contributing to partial coherence, the transmittance and reflectance of double-sided polished silicon were measured in the mid-infrared spectral region using the FT-IR spectrometer. Using double-side polished samples was critical since instrumental effects have their own characteristic influence on the spectra, independent of surface roughness. Airy's formulas for thin films (equivalent to scalar scattering theory for smooth samples) in conjunction with spectral averaging were used to predict the transmittance and reflectance. Existing tabulated data were used for the optical constants. Fitting required using thickness as a variable and the nominal thickness

as a starting value. This approach resulted in excellent agreement throughout the wavenumber range for the sample D1 measurement. Adjusting the optical constant values was needed to obtain good agreement of the fringe positions for two regions in the mid-infrared for sample D2.

Since the spectrometer averages the data points, the resolution set by the spectrometer can be treated as an averaging interval. The fringe smoothing used in the fitting process also requires an averaging interval, the coherent spectral width, which was found to be larger than the resolution of the instrument for the double-side polished sample measurements. This indicates that beam divergence and possibly nonparallel surfaces, rather than the other causes of partial coherence (finite instrumental resolution and rough surfaces) were critical in reducing the measured fringe contrast. Unlike earlier studies by other researchers, the coherent spectral width was assumed to be linearly-dependent on wavenumber, based on the assumption that the degree of coherence evident in the data is most affected by the phase shift of the incident radiation. This allowed for good fits of the fringe maxima and minima for sample D1, but may have been inadequate in the case of sample S1. The linearly dependent coherent spectral widths used for fringe smoothing confirm that the degree of coherence is wavenumber-dependent, but the exact dependence is inconclusive and can be explored further. It should be noted that the coherent spectral width assumes that a good fit of the observed transmittance is achievable, but this is not always possible. The fitting analysis also yielded reasonable values for the thickness and the index of refraction of silicon. The good agreement achieved between the calculated and measured spectra of silicon indicates that spectral averaging is an effective way to address partial coherence.

5.1.2 Effect of Rough Surfaces

The primary goal of this work is to gain an understanding of the effects of rough surfaces on the radiative properties of thin films. Scalar scattering theory, a commonly used approach to modeling the radiative properties of thin films with rough surfaces, was found to be effective for some of the samples measured in this study. The method to calculate the spectra involved using scalar scattering theory along with spectral averaging to address the partial coherence. Thickness and rms surface roughness were taken as adjustable parameters in the fitting process with tabulated data used for the optical constants. These predictions were compared with measured spectra taken using the FT-IR spectrometer.

Reasonable agreement of the transmittance was achieved for sample S4. Topographic data provided insight into the underlying causes of error in the case of samples S2 and S3. Surface statistics, such as rms roughness and autocorrelation length, were calculated using data from the AFM and the surface profilometer, and the optical microscope produced images revealing large grain-like features. These surface microstructures, which were large relative to the surface roughness of the other samples studied in this work, may have affected the transmittance in a way that scalar scattering theory could not adequately address. This is an important result and shows that how a wafer is manufactured can have a dramatic effect on the surface roughness levels and thus the radiative properties. The optical roughness is hence an important factor in determining the effectiveness of applying scalar scattering theory. Therefore, it is

concluded that limitations in the theory led to failure to obtain agreement for samples S2 and S3.

The approach for modeling the radiative properties adopted in the present work yielded excellent agreement for the transmittance of the diamond film. This was possible after considering the polycrystalline structure of CVD diamond film, which allowed for lower index of refraction values than those provided by the tabulated data. The fringe flipping predicted in the spectra was observed in the measurements. A comparison of the measured and predicted reflectance spectra showed general agreement along with shifted fringes and offsets in the mean reflectance values. Inherent limitations of the reflectance accessory when used for samples with rough surfaces may have contributed to the lack of agreement. The more likely reason involves the beam divergence since the conical-conical nature of the reflectance measurement was not accounted for in the predicted reflectance. This can be incorporated into future work using BRDF data.

5.2 Future Work

Because the microscope images suggest that the sample surface characteristics affected the radiative properties in certain cases, it is recommended that much future work be devoted toward understanding scattering at a fundamental level. Using scalar scattering theory to model the radiative properties of layers with different levels of roughness may also provide useful information. Beam divergence should be investigated further since this appears to have a dramatic impact on the partial coherence. Focusing on problems posed by measuring scattering transmissive materials, as done in a study by Hanssen and Kaplan (1998), employing an integrating sphere to directly measure

scattering, and analyzing sources of systematic error in FT-IR measurements, such as interreflection error, are additional ways to better understand the instrumental affects on the data.

Alongside this, a multiple parameter least-squares fitting program could be used to help ensure that the best possible fits are obtained with the experimental spectra. All of the curve fits in the present work were performed with a fit-by-eyes method. Least-squares fitting involves determining the best fitting parameters by minimizing the quantity chi-squared, defined as (Zhang et al., 1997):

$$\chi^2 \equiv \sum_{j=1}^{M} \left(\frac{T_m(\overline{\nu}, d_j) - T_c(\overline{\nu}, d_j, n, \kappa)}{\sigma_m} \right)^2 \tag{5.1}$$

where T_m and σ_m are the measured transmittance and its standard deviation, respectively, M is the number of data points, and T_c is the calculated transmittance. Although curve fitting is an area of error analysis that has been well studied, care must be taken that absorption is properly addressed since the error distributions may be non-Gaussian when absorption is present in the data (Grossman and McDonald, 1995). It would also be possible to compare extracted values of n and κ as functions of wavelength with the values from the tabulated data. Furthermore, the results presented in this work would benefit from an uncertainty analysis on both the experiment and the theory. By quantifying the uncertainty with error bars for the predicted and measured spectra, such an analysis may help obtain closure between experiment and theory. Through further study beginning with the recommendations discussed here, FT-IR measurements of silicon and CVD diamond film can lead to a deeper understanding of how rough surfaces affect the radiative properties of thin films.

REFERENCES

Beckmann, P., and Spizzichino, A., *The Scattering of Electromagnetic Waves from Rough Surfaces*, Artech House, Norwood, MA, 1963.

Bell, R.J., *Introductory Fourier Transform Spectroscopy*, Academic Press, New York, 1972.

Birch, J.R., and Clarke, F.J.J., Interreflection Errors in Fourier Transform Spectroscopy: A Preliminary Appraisal, *Analytica Chimica Acta*, Vol. 380, pp. 369-378, 1998.

Boueke, A., Kuhn, R., Fath, P., Willeke, G., and Bucher, E., "Latest Results on Semitransparent POWER Silicon Solar Cells," *Solar Energy Materials and Solar Cells*, Vol. 65, pp. 549-553, 2001.

Born, M., and Wolf, E., *Principles of Optics*, Pergamon Press, Oxford, United Kingdom, 1975.

Carniglia, C.K., and Jensen, D.G., "Single-Layer Model for Surface Roughness," *Applied Optics*, Vol. 41, pp. 3167-3171, 2002.

Chen, G., and Tien, C.L., "Partial Coherence Theory of Thin Film Radiative Properties," *Journal of Heat Transfer*, Vol. 114, pp. 636-643, 1992.

Coutts, T.J., "A Review of Progress in Thermophotovoltaic Generation of Electricity," *Renewable & Sustainable Energy Reviews*, Vol. 3, pp. 77-184, 1999.

Dunmore, F.J., and Hanssen, L.M., "Miniature Fourier Transform Instrument for Radiation Thermometry," *11th International Conference on Fourier Transform Spectroscopy,* pp. 415-418, 1998.

Edwards, D.F., "Silicon (Si)," in *Handbook of Optical Constants of Solids*, edited by Palik, E.D., Academic Press, Orlando, pp. 547-569, 1985.

Edwards, D.F., and Philipp, H.R., "Cubic Carbon (Diamond)," in *Handbook of Optical Constants of Solids*, edited by Palik, E.D., Academic Press, Orlando, pp. 665-673, 1985.

Farabaugh, E.N., Lai, G., Feldman, A., and Robins, L.H., "A Closed CVD System for the Deposition of Diamond Films," *Applications of Diamond Films and Related Materials: Third International Conference*, Gaithersburg, MD, pp. 361-364, 1995.

Filinski, I., "The Effects of Sample Imperfections on Optical Spectra," *Physica Status Solidi B*, Vol. 49, pp. 577-588, 1972.

Flik, M.I., and Zhang, Z.M., "Influence of Nonequivalent Detector Responsivity on FT-IR Photometric Accuracy," *Journal of Quantitative Spectroscopy and Radiative Transfer*, Vol. 47, pp. 293-303, 1992.

Fujiwara, H., Koh, J., Rovira, P.I., and Collins, R.W., "Assessment of Effective-Medium Theories in the Analysis of Nucleation and Microscopic Surface Roughness Evolution for Semiconductor Thin Films," *Physical Review B*, Vol. 61, pp. 10832-10844, 2000.

Griffiths, P.R., and de Haseth, J.A., *Fourier Transform Infrared Spectrometry*, Wiley, New York, 1986.

Grossman, E.N., and McDonald, D.G., "Partially Coherent Transmittance of Dielectric Lamellae," *Optical Engineering*, Vol. 34, pp. 1289-1295, 1995.

Hanssen, L.M., and Kaplan, S.G., "Problems Posed by Scattering Transmissive Materials for Accurate Transmittance and Reflectance Measurements," *SPIE Conference on Optical Diagnostic Methods for Inorganic Transmissive Materials*, San Diego, CA, pp. 28-36, 1998.

Kaplan, S.G., and Hanssen, L.M., "Infrared Regular Reflectance and Transmittance Instrumentation and Standards at NIST," *Analytica Chimica Acta*, Vol. 380, pp. 303-310, 1999.

Kaplan, S.G., Hanssen, L.M., and Datla, R.U., "Testing the Radiometric Accuracy of Fourier Transform Infrared Transmittance Measurements," *Applied Optics*, Vol. 36, pp. 8896-8908, 1997.

Kumar, A.R., Zhang, Z.M., Boychev, V.A., Tanner, D.B., Vale, L.R. and Rudman, D.A., "Far-Infrared Transmittance and Reflectance of $YBa_2Cu_3O_{7-\delta}$ Films on Si Substrates," *Journal of Heat Transfer*, Vol. 121, pp. 844-851, 1999.

Mahan, J.R., *Radiation Heat Transfer: A Statistical Approach*, John Wiley & Sons, New York, 2002.

Mehta, C.L., "Coherence-time and Effective Bandwidth of Blackbody Radiation," *Il Nuovo Cimento*, Vol. 28, pp. 401-408, 1963.

Mitsas, C.L., and Siapkas, D.I., "Generalized Matrix Method for Analysis of Coherent and Incoherent Reflectance and Transmittance of Multilayer Structures with Rough Surfaces, Interfaces, and Finite Substrate," *Applied Optics*, Vol. 34, pp. 1678-1683, 1995.

Modest, M.F., *Radiative Heat Transfer*, Academic, San Diego, CA, 2003.

Montecchi, M., Montereali, R.M., and Nichelatti, E., "Reflectance and Transmittance of a Slightly Inhomogeneous Thin Film Bounded by Rough, Unparallel Interfaces," *Thin Solid Films*, Vol. 396, pp. 262-273, 2001.

Petrich, R., and Stenzel, O., "Modeling of Transmittance, Reflectance and Scattering of Rough Polycrystalline CVD Diamond Layers in Application to the Determination of Optical Constants," *Optical Materials*, Vol. 3, pp. 65-76, 1994.

Poruba, A., Fejfar, A., Remes, Z., Springer, J., Vanecek, M., Kocka, J., Meier, J., Torres, P., and Shah, A., "Optical Absorption and Light Scattering in Microcrystalline Silicon Thin Films and Solar Cells," *Journal of Applied Physics*, Vol. 88, pp. 148-160, 2000.

Robins, L.H., Farabaugh, E.N., and Feldman, A., "Determination of the Optical Constants of Thin Chemical-Vapor-Deposited Diamond Windows from 0.5 to 6.5 eV," *SPIE Diamond Optics IV,* Vol. 1534, pp. 105-115, 1991.

Shen, Y.J., Zhu, Q.Z., and Zhang, Z.M., "A Scatterometer for Measuring the Bidirectional Reflectance and Transmittance of Semiconductor Wafers with Rough Surfaces," *Review of Scientific Instruments*, Vol. 74, pp. 4885-4892, 2003.

Siegel, R. and Howell, J.R. *Thermal Radiation Heat Transfer*, Taylor & Francis, New York, 2002.

Zhang, Z.M., "Optical Properties of Layered Structures for Partially Coherent Radiation," *Proc. of the 10th International Heat Transfer Conference*, Brighton, UK, pp. 177-182, 1994.

Zhang, Z.M., "Optical Properties of a Slightly Absorbing Film for Oblique Incidence," *Applied Optics*, Vol. 38, pp. 205-207, 1999.

Zhang, Z.M., "Surface Temperature Measurement Using Optical Techniques," *Annual Review of Heat Transfer*, C.L. Tien (ed.), Begell House, NY, Vol. 11, pp. 351-411, 2000.

Zhang, Z.M., "Microscale Thermal Radiation in Thin Solid Films," *International Conference on Energy Conversion and Applications*, Wuhan, China, pp. 281-286, 2001.

Zhang, Z.M., Lefever-Button, G., and Powell, F.R., "Infrared Refractive Index and Extinction Coefficient of Polyimide Films," *International Journal of Thermophysics,* pp. 905-916, 1998.

Zhang, Z.M., Fu, C.J., and Zhu, Q.Z., "Optical and Thermal Radiative Properties of Semiconductors Related to Micro/Nanotechnology," *Advances in Heat Transfer*, Vol. 37, pp. 179-296, 2003.

VITA

Vinh Khuu was born in Malaysia and grew up in the Minneapolis metropolitan area after immigrating to the US. He attended Stanford University, earning his B.S. in Mechanical Engineering in June 2002. The following fall he began his graduate studies at Georgia Tech Lorraine, the European campus of Georgia Tech located in Metz, France, and arrived at the main campus in May 2003. He has spent the past year working in Dr. Zhang's heat transfer research group. His hobbies include amateur astronomy, black and white photography, reading, and traveling. Upon completion of his studies, he wishes to pursue a career in heat transfer and thermal design.